MESH-IN: a MESHed INlet offline coupling method for 3-D extreme hydrodynamic events in DualSPHysics

Gioele Ruffini[a,*], José M. Domínguez[b], Riccardo Briganti[c], Corrado Altomare[d], Jacob Stolle[e], Alejandro J. C. Crespo[b], Bahman Ghiassi[f], Salvatore Capasso[g], Paolo De Girolamo[a]

[a]*Department of Civil, Building and Environmental Engineering DICEA, Sapienza University of Rome, Via Eudossiana 18, 00184 Rome, Italy*
[b]*EPHYSLAB Environmental Physics Laboratory, CIM-UVIGO, Universidade de Vigo, Ourense, Spain*
[c]*Department of Civil Engineering, Faculty of Engineering, University of Nottingham, Nottingham NG7 2RD, U.K.*
[d]*Department of Civil and Environmental Engineering (DECA), Universitat Politécnica de Catalunya,Jordi Girona, 08034, Barcelona, Catalunya, Spain*
[e]*Institut National de la Recherche Scientifique Eau Terre Environnement, 490 Rue de la Couronne, Quebec City, QC G1K 9A9, Canada*
[f]*School of Engineering, University of Birmingham, Birmingham B15 2TT, UK*
[g]*Environmental and Maritime Hydraulics Laboratory (LIDAM), Università degli Studi di Salerno, Via Giovanni Paolo II 132, 84084, Fisciano, Italy*

Abstract

Extreme hydrodynamic events, such as those driven by tsunamis, have a significant impact on coastal environments. The Smoothed Particle Hydrodynamics computational method gained popularity in modelling these phenomena. However, high resolution is needed in areas of interest, making coupling techniques popular to reduce computational costs. Herein, a new two-step offline coupling method was developed and validated in DualSPHysics. In step 1, the simulated velocity field and water depth are measured over a two-dimensional meshed surface of a generating domain. In step 2, the interpolated flow variables are used as boundary conditions in a receiving domain with equal or higher resolution. The method was validated by using two different laboratory experiments that are representative of tsunami propagation and inundation inland. The results show a reduction of computational time of up to 17.6 times, with decreasing savings for increasing resolution in the receiving domain. The validation tests showed that the developed method allows to simulate flows in the receiving domains at nearly the same accuracy of the generating domain while also decreasing computational time. When including debris transport, improvements in accuracy occur when doubling the resolution of the receiving domain with respect to the generating domain.

*Corresponding author
Email address: gioele.ruffini@uniroma1.it (Gioele Ruffini)

Keywords: Extreme hydrodynamic events, dam-break, inlet, impact on obstacles, DualSPHysics, offline coupling, debris transport

1. Introduction

Extreme hydrodynamic events, such as tsunamis, are becoming more and more relevant in coastal areas, particularly considering major events such as the 2004 Indian, the 2011 Tohoku and the most recent 2021 Tonga tsunamis.

The propagation of such fast flows inland is characterised by three-dimensional (3-D) processes. Additionally, the interaction of the flow with structures and waterborne debris further increases the damage, as documented by Naito et al. (2014), who analysed the effect of different classes of debris after the 2011 Tohoku tsunami in Japan.

Propagation of tsunamis inland is often studied using the analogy with dam-break flows using experimental (e.g. Chanson, 2006; Stolle et al., 2018a) and numerical methods (Ni et al., 2020; Xu et al., 2021). The dam-break analogy has high relevance in coastal and offshore engineering, e.g. for studies of green water loads on ships decks (Areu-Rangel et al., 2021).

From a numerical standpoint, extreme hydrodynamic events and associated debris transport are usually very challenging to simulate using Eulerian, meshed models since they require complex numerical strategies to adjust the mesh around structures and floating bodies. Some of these approaches recently developed are, for example, immersed boundary method (e.g. Peskin, 2002), topological changes of the mesh (e.g. Pons and Boissonnat, 2007; Gaburro et al., 2020), and overset strategies (e.g. Ma et al., 2018; Romano et al., 2020). On the other hand, Lagrangian meshless methods such as Smoothed Particle Hydrodynamics (SPH) based models (Monaghan, 1992; Violeau and Rogers, 2016) are inherently more flexible, due to the discretisation of the domain using particles, and they can provide equivalent accuracy to meshed approaches for fluid-solid interactions (González-Cao et al., 2019). Therefore SPH is considered suitable to simulate violent flows and tsunami inundation (e.g. Crespo et al., 2008; Violeau and Rogers, 2016; Heller et al., 2016; Tan et al., 2018). However, computational resources and time requirements might be prohibitive for highly detailed simulations. Two different strategies can be applied to reduce them, i.e. resolution adaptivity or coupling methods, both identified as grand challenges for SPH schemes (Vacondio et al., 2021). The former is the capability of using different domain discretisations in a single domain. In the latter, higher resolution sub-domains are restricted to areas of interest (e.g. the vicinity of a structure), and offshore boundary conditions generated by other domains simulations (using the same or a different model) are prescribed. Focusing on coupling methods, meshless models are, indeed, often coupled with another (meshed or meshless) one at a coarser resolution that resolves a larger offshore area to study. Following an established classification (see e.g. Ganju et al., 2016), model coupling can be: (a) online, when two simulations using different numerical models/domains exchange information regularly, while both simulations run, with (two-way) or without (one-way) feedback between the two; or (b) offline, when information is passed from one model/domain sequentially, using the output of one simulation as the input of another, thus allowing only one-way coupling. In both coupling types, when two domains are simulated, their resolution can be the same or different. Online coupling methods for SPH, such as with DEM (Canelas et al., 2016), which allowed the validation with experimental results of complex debris flows in DualSPHysics (Canelas et al., 2017), or the coupling with Project CHRONO (Canelas et al., 2018), which allowed for the inclusion of physical constraints for fluid structure interaction (e.g. Capasso et al., 2022), are essential for multiphysics applications. Offline coupling was used, in the context of SPH, to simulate the one-dimensional propagation of waves towards the coast by first obtaining flow variables at a suitable offshore point from another wave propagation model, e.g. SWASH (Zijlema et al., 2011), and subsequently assessing the impact on the coast with SPH solvers such as DualSPHysics (Altomare et al., 2015, 2018; Suzuki et al., 2022). The same approach was also followed by implementing inlet/outlet boundary conditions for horizontal two-dimensional (2-D) flows, e.g. Tafuni et al. (2018) in DualSPHysics (Domínguez et al., 2022) and Ferrand et al. (2017). Inlet/outlet conditions were used to generate and absorb waves directly in SPH (Verbrugghe et al., 2019). Three-dimensional cases were also recently studied, only with prescribed flow with steady direction that varied in magnitude, following a predetermined law, or by giving very simple unidirectional velocity fields (Tagliafierro et al., 2021; Novak et al., 2019). Coupling methods for SPH models that can be used for flows with 3-D features are not yet fully developed and validated.

Tsunamis propagating inland are often supercritical flows, this permits a coupled downstream domain to be disconnected from the upstream one, making it possible, for example, to use the same upstream simulation for sensitivity analysis and scenarios testing downstream. However, this boundary treatment should take into account 3-D flow characteristics and ideally be able to handle reflected flow from, e.g. lateral walls and obstacles. Furthermore, such a technique should be validated also for the case of debris pick-up and transport, in which small differences in the flow simulation generate large differences in the trajectories of the waterborne debris (Stolle et al., 2018b). To the authors' knowledge, the effect of the modelling of the boundary conditions on the simulation of debris transport is a problem that has not been studied so far.

In this study we propose and validate an offline coupling technique called MESH-IN, which can be also used as an offline variable resolution approach for the simulation of 3-D flows in DualSPHysics. The motivation of this work is the need for computational resources optimisation and for providing accurate boundary conditions to simulations of flows involving 3-D characteristics, in particular of those associated to extreme hydrodynamic events. The main novelty of this technique is the combination of the use of a 2-D meshed surface (MS) with inlet boundary conditions (Tafuni et al., 2018). The MS measures the three-dimensional flow characteristics from a simulation in a generating domain (GD), which are then used, together with the inlet boundary condition, in a receiving domain referred to as MESH-IN domain. The GD may be an 'entire', 'upstream', 'far-field', 'low-resolution' domain and the MESH-IN one may refer to a 'local', 'downstream', 'near-field', 'high-resolution' domain, depending on the context in which the model is used. MESH-IN is especially suitable for flows with three-dimensional features where reflection at the inlet is negligible, extending the capabilities of available inlet techniques for SPH models.

Two laboratory experiments representative of tsunamis propagating inland are used for validation in the present study, namely Experiment I (Kocaman et al., 2020), used to analyse the case in which the total (incident and reflected) flow variables are known, and Experiment II (Stolle et al., 2018b) focusing on the performance of the MESH-IN coupling method in reproducing the rapidly evolving flow and debris transport.

The paper is structured as follows. The numerical method used and the definition of MESH-IN are described in Section 2. Section 3 shows the results of the two laboratory experiments simulated together with the respective numericals setups. Finally, the results and assessment of the performance of MESH-IN for the two validation cases are presented in Section 4 and discussed in Section 5. The conclusions of the work are summarised in Section 6, highlighting the strengths and limitations of the proposed method.

2. Numerical method

2.1. DualSPHysics

For the present study, DualSPHysics v5.0 (Domínguez et al., 2022) is used to solve the hydrodynamics in the two validation cases and the interaction between the fluid and solid bodies in Experiment II is handled by coupling the hydrodynamic solver with Project CHRONO (Anitescu and Tasora, 2010; Tasora and Anitescu, 2011) using the Canelas et al. (2018) implementation.

2.1.1. Governing Equations and boundary conditions

DualSPHysics Domínguez et al. (2022) is based on Weakly Compressible SPH (WCSPH) with the fluid phase governed by the Navier–Stokes equations, reduced to ordinary differential equations solved in a Lagrangian framework. The conservation of mass and momentum is expressed as (Gomez-Gesteira et al. 2012; Violeau and Rogers 2016):

$$\frac{d\rho}{dt} = -\rho \nabla \cdot \boldsymbol{v}, \tag{1}$$

$$\frac{dv}{dt} = -\frac{1}{\rho}\nabla p + \boldsymbol{g} + \boldsymbol{\Gamma}, \tag{2}$$

where ρ is the fluid density, t is time, p is the pressure, $\boldsymbol{v} = (v_x, v_y, v_z)$ is the velocity vector and Γ is the dissipative term. Here a Cartesian coordinate system is used, with axes x and y along horizontal directions, and vertical coordinate z, directed upwards, therefore, $\boldsymbol{g} = (g_x, g_y, g_z)$ is the gravitational acceleration vector (here $g_x = 0,\ \ g_y = 0,\ \ g_z = -9.81$ m/s^2 is used). SPH discretises every part of the computational domain (solid and fluid) into sets of particles carrying different properties such as type, density, pressure and velocity. In general, two steps are defined to apply Eq. (1) and (2), i.e., a kernel approximation and a particle approximation (Liu and Liu, 2003). First, any variable f of a particle $a = 1, ..., N_p$ with N_p the total number of particles, located at $\boldsymbol{r_a} = (x_a, y_a, z_a)$, is represented by the integral at location $\boldsymbol{r} = (x, y, z)$ as:

$$f(\boldsymbol{r}_a) = \int_\Omega f(\boldsymbol{r}) W(\boldsymbol{r}_a - \boldsymbol{r}, h_p) d\boldsymbol{r}, \tag{3}$$

with Ω being the computation domain, W being a weighting function called smoothing kernel, which monotonically decreases with distance, and h_p being the smoothing length, which determines the size of the kernel support. In this study the Wendland (1995) kernel function was used. In the second step, the integral in Eq. (3) is approximated by interpolating the characteristics of the surrounding particles as:

$$f(\boldsymbol{r}_a) \approx \sum_{b=1}^{N_k} f(\boldsymbol{r}_b) \frac{m_b}{\rho_b} W_{ab}, \tag{4}$$

where the summation is extended to all the particles $b = 1, ..., N_k$ with N_k being the number of particles inside the kernel. In Eq. (4), $W_{ab} = W(r_a - r_b, h_p)$, and m_b and ρ_b are the mass and density of the b^{th} neighbour particle, located at $\boldsymbol{r_b} = (x_b, y_b, z_b)$. In addition, any derivative of f can be expressed as:

$$\nabla f(\boldsymbol{r}_a) \approx \sum_{b=1}^{N_k} f(\boldsymbol{r}_b) \frac{m_b}{\rho_b} \nabla_a W_{ab}, \tag{5}$$

where ∇a indicates derivation with respect to the coordinates of particle a. Eq. (1) can be rewritten in the SPH framework for a particle a as

$$\frac{d\rho_a}{dt} = \sum_{b=1}^{N_k} m_b \boldsymbol{v}_{ab} \cdot \nabla_a W_{ab} + \delta_\phi h_p c_0 \sum_{b=1}^{N_k} \Psi_{ab} \cdot \nabla_a W_{ab} \cdot \frac{m_b}{\rho_b}, \tag{6}$$

with δ_ϕ a free parameter, c_0 the speed of sound at the reference density ρ_0 of the simulation, and Ψ_{ab} the density diffusion term defined, in the present study, following Fourtakas et al. (2019). In particular, c_0 is used to ensure that the weakly compressible hypothesis of the model holds and for this reason it needs to be at least 10 times the maximum fluid velocity. c_0 is calculated, by default, as $c_0 = c_f\sqrt{gh}$, where c_f is a multiplication factor and h the total water depth. Ψ_{ab} was used to avoid density oscillations, common for SPH models, which often results in incorrect or unstable pressure at boundaries or floating bodies particles. Eq. (2) the SPH framework is written as

$$\frac{d\boldsymbol{v}_a}{dt} = -\sum_{b=1}^{N_k} m_b \Big(\frac{P_b + P_a}{\rho_b \cdot \rho_a} + \Pi_{ab} \Big) \nabla_a W_{ab} + \boldsymbol{g}, \tag{7}$$

where P_b and P_a are the pressures at the particles b and a, with ρ_b and ρ_a their respective densities. Π_{ab} groups all the dissipative terms, which are computed, for the present study, following the artificial viscosity formulation (Monaghan, 1992), since it is the most widely used one for coastal engineering applications (Vacondio et al., 2013; Tan et al., 2018). A more extensive analysis of the SPH governing equations and model can be found in the reference literature (e.g. Liu and Liu 2003; Gomez-Gesteira et al. 2010; Domínguez et al. 2022).

2.1.2. *Modified Dynamic Boundary Condition (MDBC)*

In DualSPHysics, two different boundary conditions formulations are implemented to treat solid boundary particles: the Dynamic Boundary Condition (DBC) and the Modified Dynamic Boundary Condition (MDBC). The DBC is the original formulation implemented for solid boundary conditions in DualSPHysics (Crespo et al., 2007). MDBC is an improvement of the previous DBC, which overcomes the inaccurate prediction of pressure fields near the boundary, resulting in a gap between the solid and the fluid (English et al., 2022). Additionally, as mentioned in Section 2.1.1, the density diffusion term of Fourtakas et al. (2019) was used as it is highly recommended in combination with MDBC Domínguez et al. (2022). Additionally, the velocity of the boundary particle is set to $\boldsymbol{v} = 0$ applying the no-slip condition used for DBC.

MDBC is used in the present study, due to the aforementioned advantages. This condition is applied for all surfaces, solids, and floating bodies particles that will interact with the fluid with the exception of the opening gate of Experiment II to avoid entrainment of particle during its opening. Normals to the geometrical surfaces of each solid are calculated for particles at the distance of at least $2h_p$ from it, with $h_p = k\sqrt{3}dp$ as the smoothing length, dp being the initial particle spacing, which defines the resolution, and k a multiplication coefficient. h_p is used to calculate the radius of influence of the kernel function, which is $2h_p$ in this study. This ensures that normals are defined for every boundary particle that can interact with the fluid.

2.1.3. *MESH-IN coupling method*

MESH-IN, as introduced in Section 1, is an offline coupling method that uses the flow modelled in a GD simulation on a MESH-IN domain of equal or coarser resolution. The method is organised in two steps:

Step 1 A MS is located in the GD, as shown in Fig. 1. Here, the flow variables (velocity field and the free surface) calculated in the GD are recorded onto the MS.

Step 2 The flow measurements provided by the GD are used by MESH-IN to provide the inlet conditions with the same resolution of GD, dp_{GD} or higher for the MESH-IN domain. The particles at the boundary are generated by using the open boundary of Tafuni et al. (2018) with the needed buffer zone upstream the MS (Fig. 1).

Step 1 consists in positioning the MS at a suitable position in the GD, which in the two dam-break cases in this work is parallel to the gate and across the full width of the tank at a distance $x = ldp_{\mathrm{GD}}$ (see Fig. 1), where l is a real number, from the dam-break release position. Note that multiples of dp_{GD} were used only as reference for the positioning of the MS in this study and it can be positioned everywhere is needed. The MS is a regular mesh and consists of N_j nodes that are $\Delta_{MS} = ndp_{GD}$ spaced from each other, in y and z-directions where $n \leq 1$ and is real number. The MS spacing in both x and y-directions may be different, however for simplicity it coincides in this study. The resolution of the MS does not need to match dp_{GD} or the particle spacing of the MESH-IN simulations $dp_{MESH-IN}$, although $dp_{MESH-IN} \approx \Delta_{MS}$ should be chosen to avoid loss of accuracy during interpolation. Due to this, in the present study $dp_{MESH-IN} = \Delta_{MS}$. Subsequently, during the GD simulation the velocity $\boldsymbol{v}_j$ is calculated for each node of the MS with the following relationship

$$\boldsymbol{v}_j = \frac{\sum_{b=1}^{N_k} \boldsymbol{v}_b W_{jb}}{\sum_{b=1}^{N_k} W_{jb}}, \tag{8}$$

where $j = 1, ..., N_j$ and $\boldsymbol{v}_j$ are the velocity vectors for each node. To track the free surface position the value of the mass of a specific j^{th} node m_j is computed using the mass values of all neighbouring fluid particles. The free surface position is then located where

$$m_j = \sum_{b=1}^{N_k} m_b W_{jb} = m_{lim} m_{ref} \tag{9}$$

by linear interpolation between two consecutive nodes in z-direction. Here m_{lim} is a multiplication factor between 0.4 and 0.5 that determines the ratio of fluid particle inside the influence area of the chosen point. A typical value for 3-D simulations is $m_{lim} = 0.5$. m_{ref} is the mass value of a fluid particles calculated as ρdp^3 in 3-D, where ρ is he fluid density.

Step 2 uses the aforementioned measured variables to apply Tafuni et al. (2018) boundary condition. To do that, this open boundary condition uses a buffer zone built upstream the mesh (Fig. 1) made of buffer particles. The width of the buffer zone is chosen to ensure full kernel support for the particles near this open boundary boundary, thus a thickness of 8 $dp_{MESH-IN}$ is used. In this zone the velocity field and the free water surface elevation are computed by bilinear and linear interpolation, respectively, from the values stored in the MS nodes during the GD simulation, while the pressure and density are extrapolated from the fluid particles using ghost nodes following the Liu and Liu (2006) method. Additionally, an algorithm that converts the fluid particles entering the buffer area in buffer particles, instead of discarding them from the simulation, is used. This avoids unphysical draining of the fluid when the flow is reflected back into the inlet buffer.

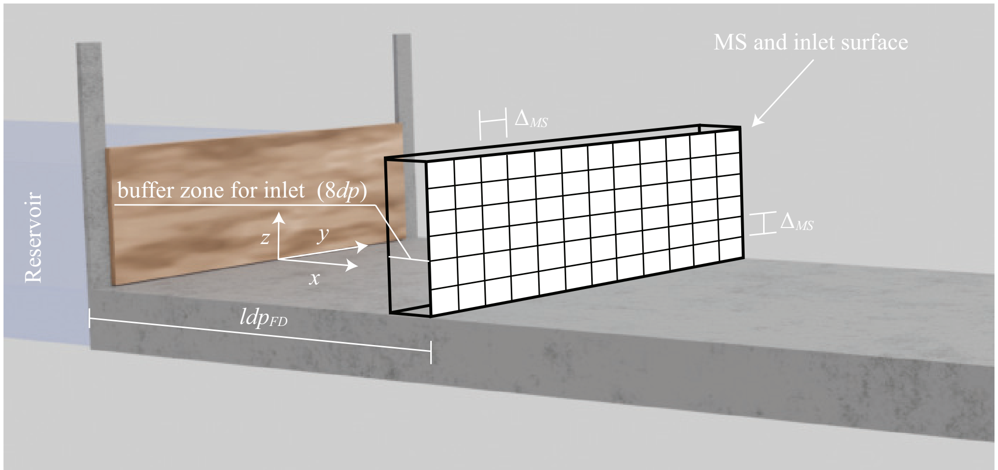

Figure 1: Scheme of the setup for a generic MESH-IN Boundary condition.

Note that any downstream influence of the flow at the MS position (e.g. subcritical conditions, reflection from obstacles) is taken into account in the interpolated velocity field and depth of the GD simulation. However, any change of these processes in the MESH-IN domains simulated in Step 2 is not considered in the boundary conditions. Therefore, this technique, when changing conditions downstream of the MS, e.g. structures position, is suitable for scenarios in which the boundary is considered not affected by any change in the processes occurring downstream. Note that, MESH-IN aims at saving computational resources, thus allowing more detailed simulations or allowing simulations that would not be otherwise possible. Since the boundary conditions are obtained by interpolation on a MS, it is not expected from this method to lead to more accurate results in the MESH-IN domain than the GD simulation.

Finally, due to the very high parallelisation of the processes with the use of Graphics Processing Units (GPUs) the distribution of the work amongst processing cores might change between two executions of the same simulation. This in turn may lead to different round-off numerical differences, which slightly affect the results of the simulations. These differences would be similar to random error in repeated physical experiments. Round-off numerical differences in the solver occur when changing the order of the mathematical floating-point operations, as the precision of real numbers is always limited. The particles are grouped into cells for efficiency reasons (Domínguez et al., 2011, 2013), however when a specific task is run in parallel, the order of the particles within each cell may vary. Other processes may also change the order of the calculation of the interaction between the particles. Changing this also modifies the set of particles that each computation unit processes and the partial results that must then be combined into a final result. For this reason, during the initialisation of the DualSPHysics solver, it was ensured that the particles are always ordered in the same way and that the distribution of work between the calculation units does not change either. This option implies a slight runtime overhead (less than 1%), but ensures perfect repeatability of the numerical simulations.

2.2. CHRONO Engine

The dynamics of the debris in the Stolle et al. (2018b) experiment is solved using, the coupling between DualSPHysics and the multi-physics engine Project CHRONO (Canelas et al. 2018). This solver (Tasora and Anitescu, 2011; Anitescu and Tasora, 2010) is able to consider multiple types of structural constraints and also to solve collisions through two alternative formulations, (i) Non-SMooth Contacts (NSMC), which considers fully rigid impacts, and (ii) SMooth Contacts (SMC) which solves deformable contacts and is used here. The introduction of this coupling helped testing the accuracy of the forces applied to a floating body also when using the MESH-IN method. The application of Project CHRONO for the specific case analysed here, along with the coupling mechanisms, is already discussed in Ruffini et al. (2021).

3. Validation cases

3.1. Laboratory Setups

To validate the MESH-IN method and assess its performance, the two different experimental setups introduced in Section 1 were simulated.

3.1.1. Laboratory setup for Experiment I

Experiment I consisted in a three dimensional dam-break conducted in a 1.00 m $\times$ 0.50 m rectangular basin with all the sides, including the bottom, made of glass. The area modelled herein is shown in Fig. 2. Inside the basin two walls 0.01 m thick were positioned at $x = 0.0$ m creating a 0.1 m opening in the middle, where a vertically opening gate was placed. This created a reservoir with initial water depth of $h_0 = 0.15$ m. The acrylic gate was 0.10 m wide and 3 mm thick, and had its centre positioned at the centre of the basin in y-direction ($y = 0.25$ m). The gate was lifted with a system of weights and steel ropes, resulting in a complete opening over the 0.15 m depth in 0.06 s, thus achieving an opening velocity high enough not to affect the flow (Lauber and Hager, 1998). A prismatic shaped obstacle, with rectangular horizontal cross section sides of 0.15 m and 0.08 m, was located at $x = 0.26$ m. The obstacle was placed with its main axis rotated of 28.0724° so that one of its diagonals was aligned with the x-direction at $y = 0.25$ m (see Fig. 2). Only the water depth of the flow was measured in the experiments at wave gauges (WG) placed as shown in Fig. 2b with their coordinated summarised in Table 1.

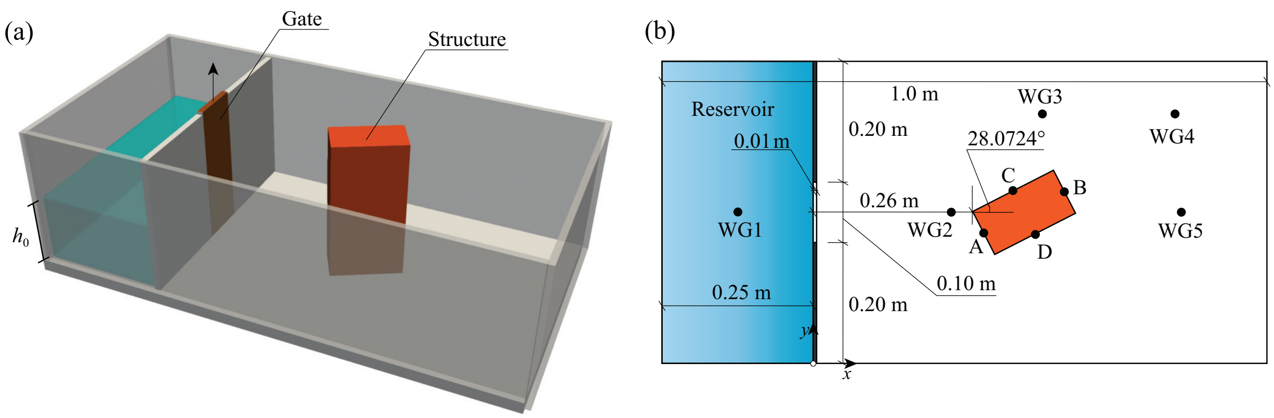

Figure 2: Numerical domain for Experiment I in (a) 3-D and (b) top view.

Table 1: WGs coordinates of Experiment I.

	x (m)	y (m)
WG1	-0.125	0.25
WG2	0.26	0.25
WG3	0.36	0.40
WG4	0.6	0.40
WG5	0.61	0.25

3.1.2. Laboratory setup for Experiment II

Experiment II consisted of a dam-break flow impacting a single scaled debris placed initially on a dry flat concrete bottom. The experiment was conducted in a 30 m × 1.5 m flume, part of which was used as a 21.55 m long reservoir with initial depth with $h_0 = 0.4$ m. The dam-break was generated by releasing the water via a swing gate. The flow propagated on an 8.45 m long test area with the horizontal concrete floor elevated by 0.2 m from the flume bottom with a structure placed at 7.03 m from the gate. The swing gate structure consisted of two 0.05 m $\times$ 0.05 m metal columns with an additional 0.03 m ledge towards the inside of the flume covered in rubber to ensure a watertight seal. This resulted in a 0.08 m protrusion on each side of the gate, slightly obstructing the dam-break flow and generating 3-D flow features (Stolle et al., 2018a). The area modelled herein is shown in Fig. 3. Note that $x = 0$ is the initial position of the waterfront and that the $y-$coordinate is rotated of 180° with respect to the one from Stolle et al. (2018b). Here, only the case with the debris positioned with its longer axis perpendicular to the flow is analysed. The debris was positioned by hand before every experimental run and centred to the flume width resulting in a mean position of the geometric centre of $x = 3.2010$ m and $y = -0.0225$ m. The trajectories of the debris were measured using a camera-based object-tracking system (Stolle et al., 2018b) and this data was used in the comparison with the simulated ones. Three wave gauges were used, namely: WG1 ($x = -0.1$ m), WG2 ($x = 2.0$ m), both along the axis of the flume, and WG3 ($x = 3.2$ m) at 0.14 m from the wall of the flume as shown in Fig. 3.

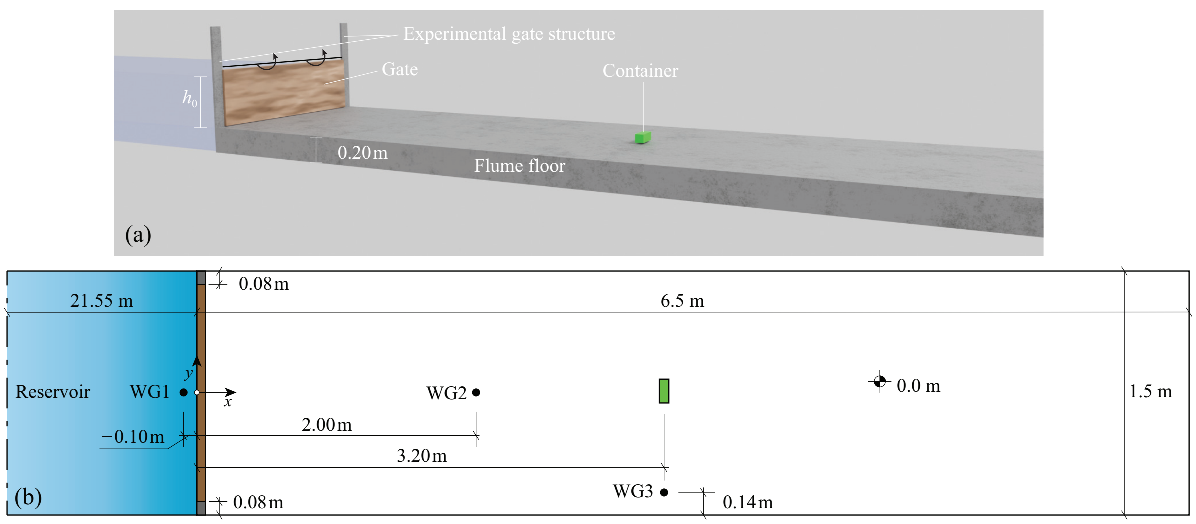

Figure 3: Numerical domain for the Experiments II in (a) 3-D and (b) top view.

3.2. Numerical setups

For each validation case, two sets of simulations were carried out. The first set consisted in the GD simulation of the experiment. In the second one, the MESH-IN method was used; for Experiment I the location of the MS and dp were varied, while for Experiment II only the location of the MS was varied. In this section, the numerical setups for both experiments are described together with the test developed to validate and assess the accuracy of the MESH-IN method. All simulations for Experiment I were carried out on a Windows workstation equipped with a NVIDIA RTX A6000 48 GB, Intel i5-12600k and 64 GB of Random Access Memory (RAM) while the simulations for Experiment II were carried out in a Windows workstation equipped with a NVIDIA RTX A5000 24 GB GPU, Intel i7-10700K and 32 GB of RAM. For Experiment I 5 s of simulated time resulted in approximately 3 h of computing time, for Experiment II 3.5 s resulted in 13 h of computing time applying the coupled DualSPHysics-Project CHRONO models.

3.2.1. Numerical setup for Experiment I

The GD investigated for Experiment I is shown in Fig. 2 was used for which the numerical setup of Capasso et al. (2021), with some modifications in the modelling of the obstacle. Note that this was considered smooth and rigid in all simulations. Additionally, the total unfiltered pressure P acting on the obstacle was computed only numerically in the A, B, C and D points indicated in Fig. 2b. The dam-break was initiated by modelling the experimental gate vertical opening mechanism by using the acceleration of the experimental gate obtained from Kocaman et al. (2020).

All the solid boundaries, including the gate, were modelled with MDBC (English et al., 2022, Section 2.1.2). For the GD $dp_{\mathrm{GD}} = 0.0025$ m was chosen, following the highest resolution investigated in Capasso et al. (2021) and resulting in 3.3×10^6 particles. Here, k= 1.2 was chosen, which resulted in a closer match with the experiments at WG5 in Capasso et al. (2021). The artificial viscosity parameter between fluid particles was $\alpha_{ff} = 0.005$, determined after initial calibration (Altomare et al., 2021) to ensure the best correspondence between simulations and experiments. The viscosity between fluid and boundary particles, $\alpha_{bf} = visc_{bf} \times \alpha_{ff}$, with $visc_{bf}$ being a multiplication factor, was kept such that $\alpha_{bf} = 0.5\alpha_{ff}$. All the numerical parameters used are summarised in Table 2.

Table 2: Parameters and formulations used for the GD simulation of Experiment I.

Parameter	**Value**
dp_{GD}	0.0025 m
ρ_0	1000 kg/m^3
c_0	24.06 m/s
k	1.2
h_p	0.0051
α_{ff}	0.005
$visc_{bf}$	0.5

A series of numerical simulations of Experiment I was carried out to assess the capabilities of the MESH-IN method; the test table of this is shown in Table 3. Note that the positions where the MS was placed and the Δ_{MS} used are scaled with dp_{GD}.

Table 3: Tests table for the application of MESH-IN for Experiment I.

$\boldsymbol{l}$	$\boldsymbol{n = \Delta_{MS}/dp_{GD}}$	**Measuring frequency of MS (Hz)**
-40	1	1000
0	1	1000
40	1, 0.5, 0.25	1000, 500, 100
80	1	1000

3.2.2. Numerical Setup for Experiment II

The full numerical domain used for Experiment II is shown in Fig. 3. This is a significantly improved version of the numerical setup of Ruffini et al. (2021), where only the first 6.50 m of the experimental area were modelled and the structure present in the experiments was not included to focus the validation test on the debris kinematic. Herein, only the case with initial impoundment depth of $h_0 = 0.4$ m was numerically investigated. The dam-break was initiated by a gate that was modelled after Stolle et al. (2018b) and opened by using the opening angle time series averaged over the experiments repetitions. The gate was kept closed for 0.5 s at the start of the simulation to let the particles stabilise, all the results are presented with $t = 0$ s at the opening of the gate. Also, all solid boundaries were modelled with MDBCs unlike in Ruffini et al. (2021) where only DBCs were used. MDBCs was not used only for the gate, due to stability issues of the simulation. This did not substantially impact the flow modelling due to the very fast opening. $dp_{\mathrm{GD}} = 0.01$ m was chosen following Ruffini et al. (2021), resulting in 28.8×10^6 particles. Note increasing resolution, such as

$dp_{\mathrm{GD}}/2$, was not possible with the current hardware making this case a perfect candidate for the application of MESH-IN. Here, k= 1.2 was used since it is the most utilised for many dam-break flows applications (Crespo et al., 2008; Capasso et al., 2021). For this numerical setup, α_{ff} was set equal to 0.0035 after initial calibration to ensure the best correspondence between simulations and experiments. For MESH-IN simulations with higher resolution than for the GD this value was recalibrated for the specific resolution (Table 4) as suggested by Altomare et al. (2021). The viscosity between fluid and boundary particles α_{bf} was kept such that $\alpha_{bf} = visc_{bf}\alpha_{ff}$ with $visc_{bf} = 0.5$. All the numerical parameters and formulations used are summarised in Table 4.

Table 4: Parameters and formulations used for the GD of Experiment II.

Parameter	**Value**
dp_{GD}	0.01 m
ρ_0	1000 kg/m^3
c_0	48.11 m/s
k	1.2
h_p	0.021 m
α_{ff}	0.0035 (0.004 after calibration for n=0.5)
$visc_{bf}$	0.5

The characteristics of the materials used for the debris and the flume floor are summarised in Table 5, where E is the Young's modulus, ν is the Poisson ratio, K is the restitution coefficient and f_c is the kinematic friction coefficient. The representative values of the actual materials used in the experiments were considered with a High Molecular Weight Polyethylene (HMWPE) for the debris and concrete for the flume floor (Harper, 2000; Michael, 1991). These values were already calibrated for the numerical setup in Ruffini et al. (2021), who also modelled the inertia of the debris using a high resolution simulation. This was necessary due to the uneven mass distribution of the experimental debris caused by the instrumentation placed inside it. For this reason, the inertia matrix is given as an input in the numerical simulations.

Table 5: Materials characteristics for the debris and flume floor for Experiment II, following Ruffini et al. (2021).

Property	**debris (HMWPE)**	**Flume floor (Concrete + Sand Paint)**
E (GPa)	0.8	30
ν (-)	0.4	0.2
K (-)	0.7	0.7
f_c (-)	0.15	0.3

Similarly to Section 3.2.1, Table 6 shows the test conditions for Experiment II. Unlike Experiment I, $x = 0dp_{\mathrm{GD}}$ and $x = -40dp_{\mathrm{GD}}$ are not used for the MS location in this case. In fact, due to the characteristics of this layout, a vertical step where the gate was placed would interfere with the MESH-IN if this was located at or upstream of the gate.

Table 6: Tests table for the application of MESH-IN for Experiment II.

$\boldsymbol{l}$	$\boldsymbol{n = \Delta_{MS}/dp_{GD}}$	**Measuring frequency of MS (Hz)**
20	1, 0.5	1000
40	1, 0.5	1000
60	1, 0.5	1000
80	1, 0.5	1000
100	1, 0.5	1000

3.2.3. Quantification of model performance

Model performance is quantified in terms of nRMSE. For variables that have dimensions of length (e.g. h) nRMSE$_l$ is calculated as

$$\mathrm{nRMSE}_l = \frac{\sqrt{\frac{1}{\mathrm{N}}\sum_{\mathrm{i}}^{\mathrm{N}}\left(\xi_{n,\mathrm{i}} - \xi_{e/GD,\mathrm{i}}\right)^2}}{h_0}, \tag{10}$$

where $\xi_{n,i}$ and $\xi_{e/GD,i}$ represent any sample of one of the numerically modelled and experimental or GD simulation variables, respectively, and N is the number of samples. For the pressure P, nRMSE$_p$ is calculated as

$$\mathrm{nRMSE}_p = \frac{\sqrt{\frac{1}{\mathrm{N}}\sum_{\mathrm{i}}^{\mathrm{N}}\left(P_{MESH-IN,\mathrm{i}} - P_{GD,\mathrm{i}}\right)^2}}{P_{idro}}, \tag{11}$$

where $P_{MESH-IN,i}$ and $P_{GD,i}$ represent the MESH-IN and the GD measured P, respectively, with P_{idro} the hydrostatic pressure calculated when the GD simulation reaches quiescence again after the dam-break. Finally, the accuracy of the simulated x and y-velocity components of the debris (v_x and v_y, respectively) is assessed with a root mean square error normalised with the shallow water flow velocity (nRMSE$_v$) as

$$\mathrm{nRMSE}_v = \frac{\sqrt{\frac{1}{\mathrm{N}}\sum_{\mathrm{i}}^{\mathrm{N}}\left(v_{n,\mathrm{i}} - v_{e,\mathrm{i}}\right)^2}}{\sqrt{gh_0}}, \tag{12}$$

where $v_{n,i}$ and $v_{e,i}$ represent the numerical and experimental velocity components, respectively, in either x- or y-directions.

4. Results

4.1. Numerical results for Experiment I

A qualitative analysis of the results is carried out by inspection of Fig. 4. Here video stills from Kocaman et al. (2020) (Fig. 4a,b,c) are shown side by side with the results of the GD (Fig. 4d,e,f) and MS at $x = 20dp_{\mathrm{GD}}$. The different snapshots have been chosen to show different stages of the flow. At the early stage of the dam-break (t = 0.1 s, Fig. 4a,d,g) the differences between GD results and those obtained using MESH-IN are visually not distinguishable. Both simulations slightly underestimate the propagation speed of the dam-break. At a later stage (t = 0.4 s, Fig. 4b,e,h), the flow is influenced by the presence of the structure and the flow features created by the flow-obstacle interactions are described by the model consistently with the experiment. In the simulation using MESH-IN, a wake bore (visible in the lower part of panels b,e,h) is less developed. Both in GD and MESH-IN simulation the simulated fronts appears in delay with respect to the experimental front. At a later stage, the visual difference between the two simulations is less evident and is limited to the details of the interactions between the incident and reflected flow near the downstream wall. Note that, when the reflected flow reaches the MS location, reflected particles are sent out of the domain.

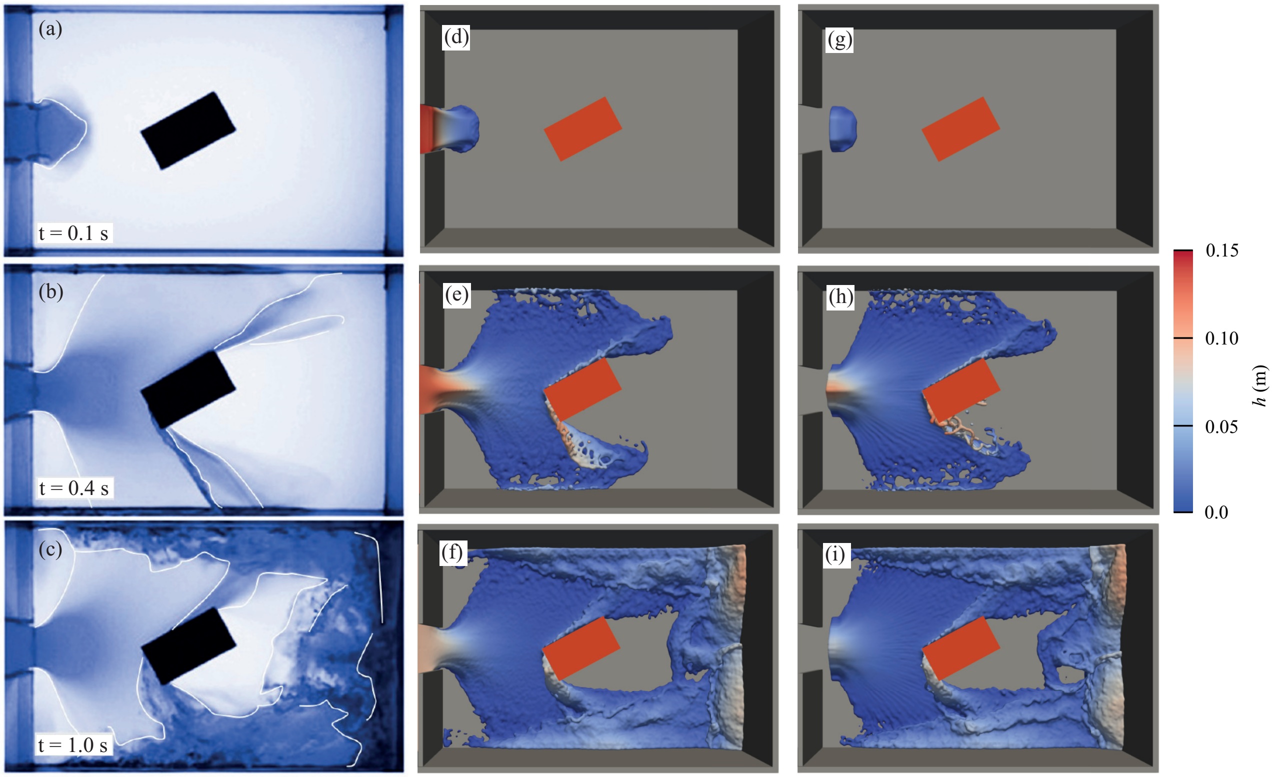

Figure 4: Comparison of the flow characteristics between Experiment I laboratory results (a,b,c), the GD simulation (d,e,f) and a simulation using MESH-IN with the MS at $x = 20dp_{GD}$ (g,h,i) at different times. The reservoir is not included as the focus is on the 3-D characteristics of the flow.

The measurements of h at WGs allows for a quantitative analysis of the results. Fig. 5 shows h/h_0 for the four WGs defined in Table 1. Here, we show MESH-IN simulations conducted with MS at different locations and all carried out using $n = 1$. Only the results for the closest and furthest MS from the gate are shown for ease of read since all the results are often overlapping, making the differences between the results difficult to be identified. nRMSE$_l$ values are calculated for all the tested locations to give a quantitative measurement of the performance of MESH-IN. At WG2 the differences among the simulations results are very small (see Fig. 5a), until approximatively $t = 2.2$ s, when the flow reflected from the walls of the domain reaches the WG. After the arrival of the reflected flow, the MESH-IN simulations are very close to each other and to the GD results with some differences at WG4, where the largest differences are found for 1.4 s $< t <$ 1.6 s (see Fig. 5c). Additionally, all results, i.e. GD and MESH-IN, have a consistent slight delay of the bore arrival at

WG5 (see Fig. 5b).

The nRMSE$_l$ is calculated for each simulation with respect to the experimental results and, nRMSE$_l$ is also calculated to compare the MESH-IN with the GD simulations (used as reference), see Table 7. Values for MS positioned at $x = -40dp_{\mathrm{GD}}$ are not shown since its placement before the gate led to a large delay in flow movement as velocities different from 0 m/s were recorded after the actual gate opening. The nRMSE$_l$ values highlight how the performance are very similar for the GD and MESH-IN simulations with a slight decay with the distance of the MS for the latter. It can be seen that the results differences between MESH-IN and GD simulations are constant or they slightly increase with the distance of the GD from the gate. This can be noted especially for WG4.

Table 7: nRMSE$_l$ values for Experiment I comparing simulations with experimental results and MESH-IN with the GD simulations results.

	WG2	**WG3**	**WG4**	**WG5**
Comparison with experiment				
GD	0.035	0.025	0.042	0.033
$x = 0dp_{\mathrm{GD}}$	0.035	0.027	0.054	0.030
$x = 20dp_{\mathrm{GD}}$	0.036	0.024	0.046	0.038
$x = 40dp_{\mathrm{GD}}$	0.040	0.027	0.058	0.038
$x = 80dp_{\mathrm{GD}}$	0.033	0.023	0.035	0.031
Comparison between MESH-IN and GD				
$x = 0dp_{\mathrm{GD}}$	0.014	0.022	0.032	0.020
$x = 20dp_{\mathrm{GD}}$	0.013	0.027	0.032	0.028
$x = 40dp_{\mathrm{GD}}$	0.015	0.025	0.035	0.029
$x = 80dp_{\mathrm{GD}}$	0.013	0.020	0.028	0.023

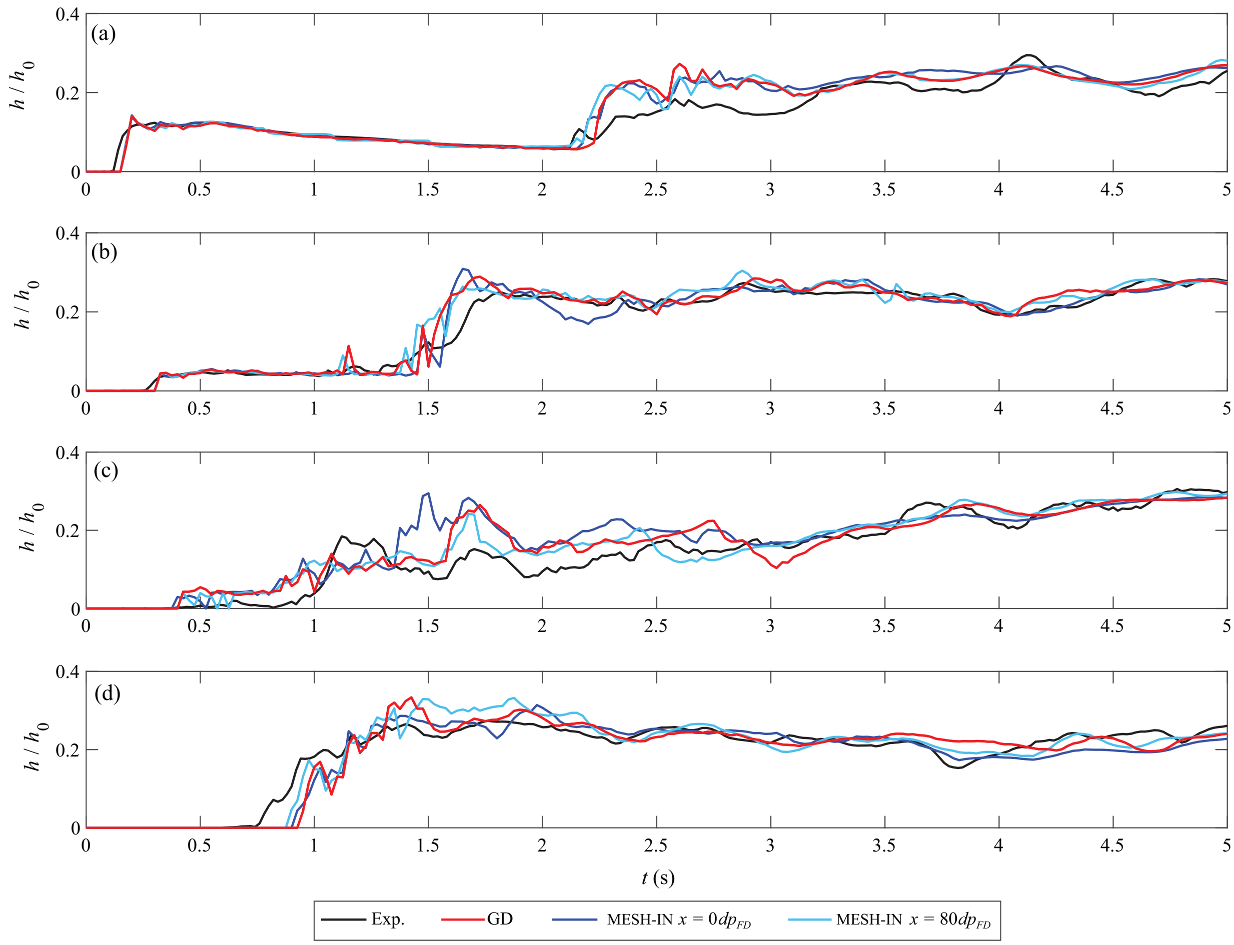

Figure 5: Comparison of $h/h0$ between Experiment I laboratory results, GD and MESH-IN simulations with m = 1 at WG2 (a), WG3 (b), WG4 (c) and WG5 (d) positions.

Fig. 6 shows the comparison for the time series of the unfiltered P at the four measurement points A, B, C and D (Fig. 2b) positioned at the centre of each face at $z = 0.02$ m for GD and MESH-IN simulations. Note that experimental pressure time series were not available. The comparison of the results for pressure is intended to: a) show the physical consistency of the results by confirming return to quiescence and b) show the relative performance of the different MESH-IN locations compared to the GD simulation. Results with MESH-IN are similar to the GD ones, with only those with the MS at $x = 80dp_{\mathrm{GD}}$ significantly differing at point B for $2 < t < 3$ s and point D for $1.25 < t < 2$ s. In this interval, the MESH-IN simulation with $x = 80dp_{\mathrm{GD}}$ reaches values close to hydrostatic pressure later than the GD simulation due to small differences in the reflected flow modelling. The hydrostatic pressure is calculated when quiescence of the GD simulation is reached, at approximatively $t = 15$ s (not shown in the figure). nRMSE$_p$ values are summarised in Table 8 for all four points. The values are very similar for all MS positions with the highest value of nRMSE$_p = 0.25$ for $x = 0dp_{\mathrm{GD}}$ at point A.

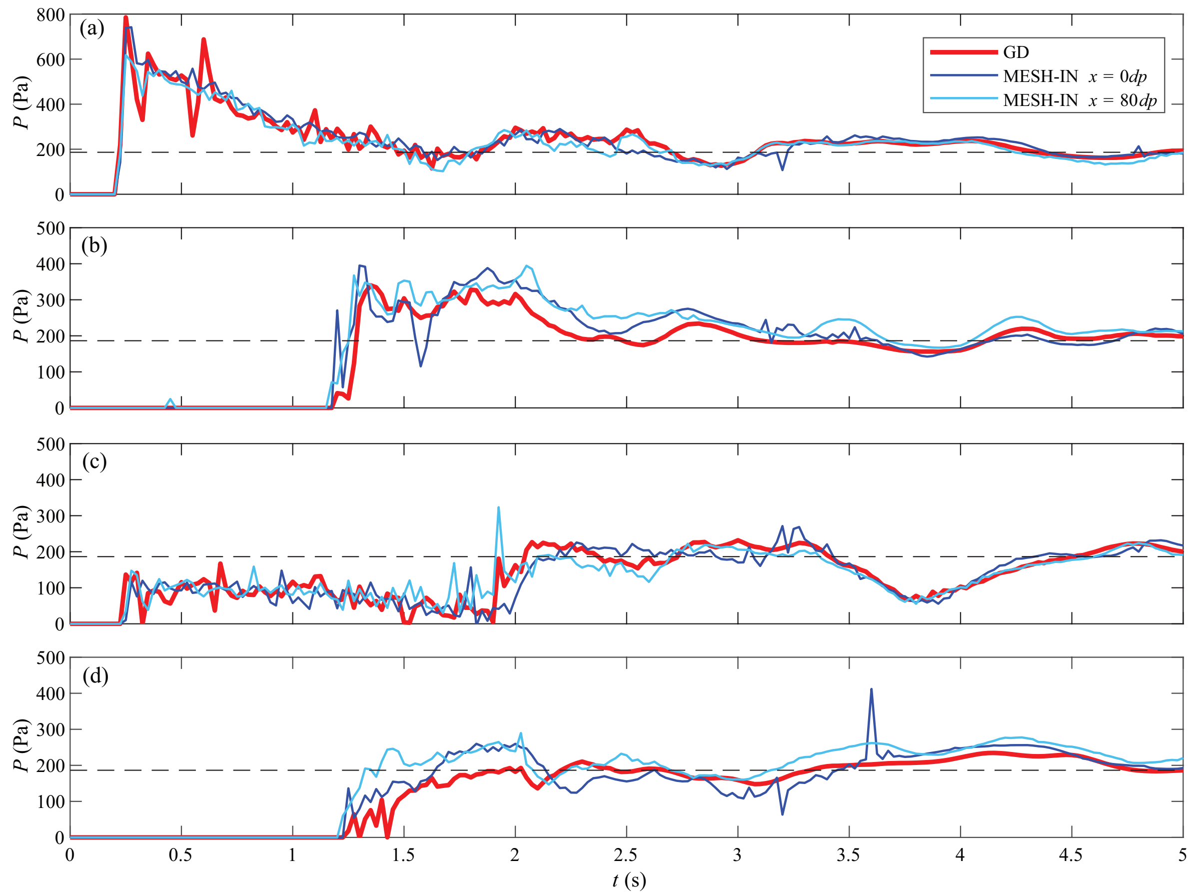

Figure 6: Comparison of the pressure time series at the points A (a), B (b), C (c) and D (d) between full and MESH-IN simulations. The value of hydrostatic pressure at quiescence of the fluid after the dam-break is represented by a horizontal dashed black line.

Table 8: nRMSE$_p$ values for Experiment I comparing MESH-IN results with the GD simulation.

	A	**B**	**C**	**D**
$x = 0dp_{\mathrm{GD}}$	0.25	0.21	0.18	0.20
$x = 20dp_{\mathrm{GD}}$	0.21	0.18	0.17	0.14
$x = 40dp_{\mathrm{GD}}$	0.18	0.24	0.15	0.13
$x = 80dp_{\mathrm{GD}}$	0.22	0.23	0.17	0.25

The sensitivity of the results to the change of $dp_{MESH-IN}$, which coincides with Δ_{MS} in this study, is shown in Fig. 7. Here MS is located at $x = 40dp_{\mathrm{GD}}$ in all simulations using this method. Results for MESH-IN are very similar to the GD ones at the arrival of the dam-break tip at WG2, 3, and 4 (see Fig. 7a,b, and c). However, the flow reflected from the obstacle and the tank walls in the MESH-IN (see e.g. Fig. 7b for 1.5 s $< t <$ 2 s and Fig. 7d for 1 s $< t <$ 1.5 s) show some apparent noise caused by spurious discontinuities among particles. Note that the tracking algorithm used to define the water in Experiment I identifies the free surface by finding the top of a continuous water column from the bottom, thus excluding discontinuities and spray.

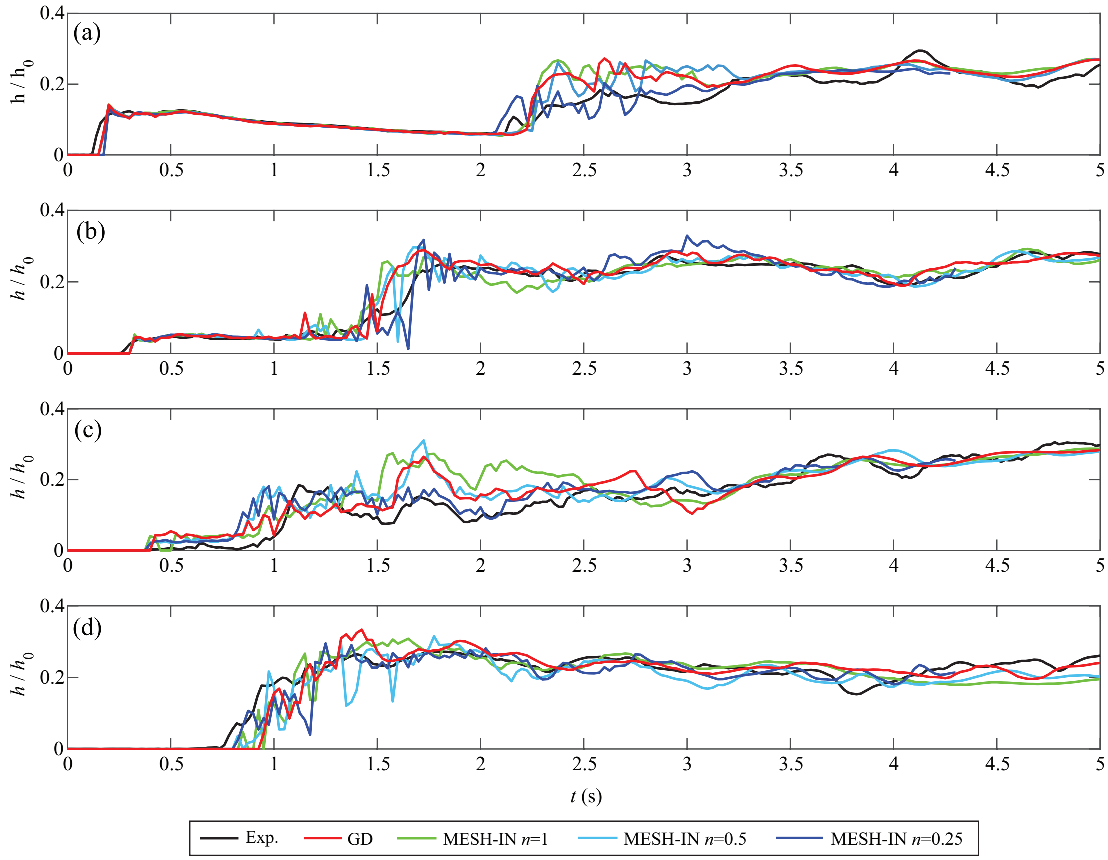

Figure 7: Sensitivity analysis on the effect of decreasing m in the MESH-IN simulations on the results for h WG2 (a), WG3 (b), WG4 (c) and WG5 (d) positions. In all MESH-IN simulations, the MS is located at $x = 40dp_{\mathrm{GD}}$.

398 *4.2. Numerical results for Experiment II*

399 For Experiment II, both the hydrodynamics and the debris kinematics are presented. This experimental setup was chosen due to the absence of a downstream wall or reflective obstacle allowing to apply always the incident flow condition at the MS locations. Fig. 8 shows h/h_0 at the three WGs for which data are available. Both the results from different locations of the MS for $n = 1$ (Fig. 8b,d) and $n = 0.5$ (Fig. 8c,e) are presented. Only the results of MESH-IN simulations with the MS at positions resulting in the highest and lowest performance, i.e. nRMSE$_l$, are shown in the figures for clarity. The water depth time series appear very similar in all cases, with notable differences between experimental and numerical results at WG2 and WG3. At WG2 all simulations overestimate h/h_0, as also reported in Ruffini et al. (2021), but the introduction of a more refined

numerical setup here results in closer match.

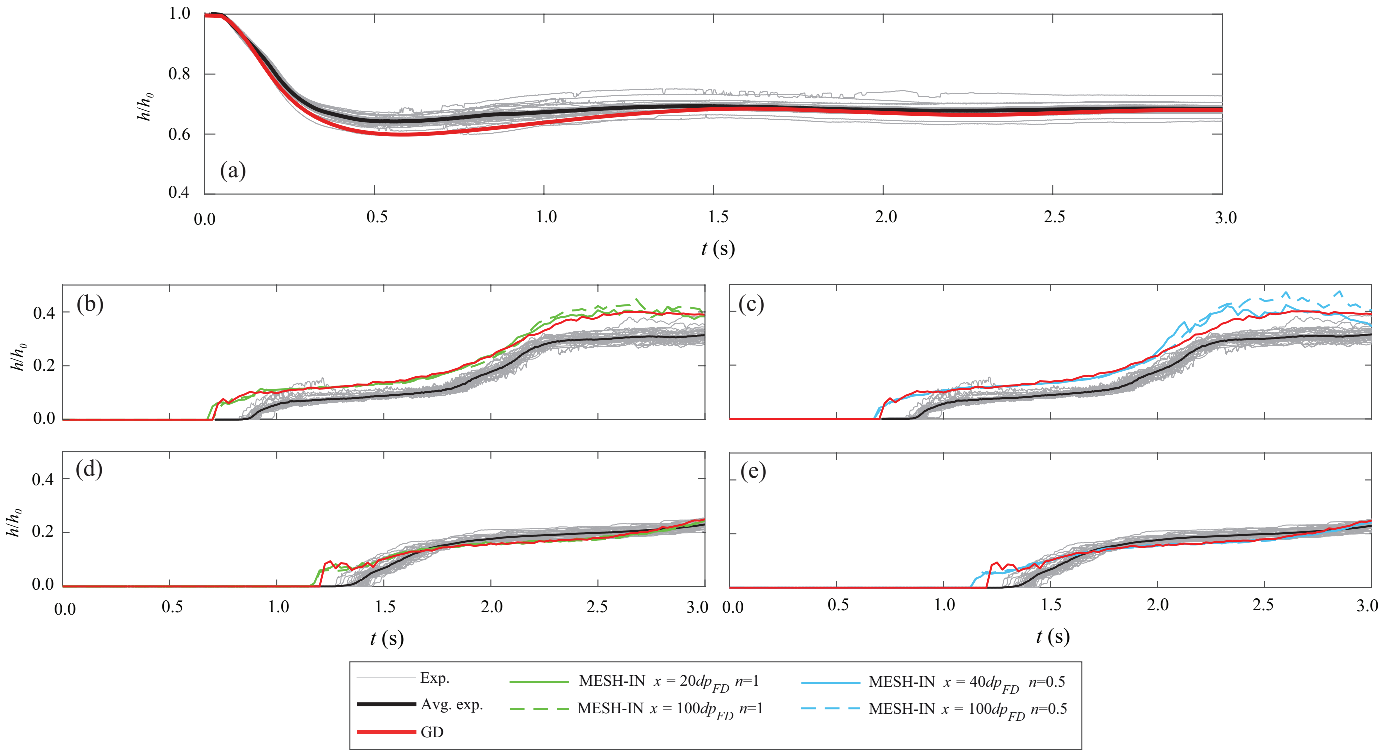

Figure 8: Comparison of $h/h0$ between experimental, GD and MESH-IN simulation results at WG1 (a), WG2 with n=1 (b), WG2 with n=0.5 (c), WG3 with n=1 (d) and WG3 with n=0.5 (e). Only the MESH-IN results with overall highest and lowest nRMSE$_l$ are shown to enhance clarity of the figure.

Overall, the performance of the MESH-IN and GD simulations are similar in terms of nRMSE$_l$ (Table 9), with a slight increase in value of the former one with the distance of the MS position. The only significant difference between GD and MESH-IN results is the slightly noisier h/h_0 at the tail of the flow ($t > 2.2$ s) for the latter at WG2 especially for Fig. 8c. This is associated to the fact that the GD simulation results are always interpolated on a mesh. However, this noise is not present at WG3, i.e. at the x position of the debris at impact, hence it does not affect the tip of the dam-break and the debris transport.

Table 9: nRMSE$_l$ values for Experiment II comparing simulations with experimental and MESH-IN results with the GD simulation.

	WG1	**WG2**	**WG3**	**WG2**	**WG3**
	Comparison with experiment			Comparison MESH-IN with GD	
GD	0.020	0.042	0.025	-	-
$x = 20dp_{\mathrm{GD}}$, $n = 1$	-	0.045	0.025	0.010	0.007
$x = 40dp_{\mathrm{GD}}$, $n = 1$	-	0.047	0.026	0.011	0.009
$x = 60dp_{\mathrm{GD}}$, $n = 1$	-	0.048	0.027	0.011	0.010
$x = 80dp_{\mathrm{GD}}$, $n = 1$	-	0.055	0.027	0.016	0.009
$x = 100dp_{\mathrm{GD}}$, $n = 1$	-	0.064	0.026	0.026	0.009
$x = 20dp_{\mathrm{GD}}$, $n = 0.5$	-	0.054	0.024	0.032	0.008
$x = 40dp_{\mathrm{GD}}$, $n = 0.5$	-	0.047	0.025	0.019	0.009
$x = 60dp_{\mathrm{GD}}$, $n = 0.5$	-	0.047	0.025	0.021	0.008
$x = 80dp_{\mathrm{GD}}$, $n = 0.5$	-	0.056	0.026	0.023	0.009
$x = 100dp_{\mathrm{GD}}$, $n = 0.5$	-	0.064	0.025	0.026	0.009

Additionally, the computational time performance of the simulations is analysed by comparing number of particles generated and computational time for the MESH-IN simulations with the GD one. The values for Experiment II are presented in Table 10. MESH-IN always reduces both computational time and maximum number of fluid particles even when using $n = 0.5$. This resulted in a maximum time reduction of 17.6 times and a reduction of fluid particles of 23.5 times for $n = 1$ while this values decrease with higher resolutions of MESH-IN simulations to 2.52 and 2.94 times for the computational time and particles reduction, respectively. This highlights how the proposed coupling method is capable of substantially decreasing the need for high computational resources while maintaining high accuracy of the results with respect to experimental and GD results. Additionally mass and total energy retainment between GD and MESH-IN simulation was demonstrated, showing essentially identical time series in three different locations along the flume (Appendix A).

Table 10: Computational times and maximum number of fluid particles generated for GD and MESH-IN simulations.

	Computational time (hours)	**Maximum number of fluid particles**
GD	13.11	19.30×10^6
$x = 20dp_{\mathrm{GD}}$, $n = 1$	0.89	1.01×10^6
$x = 40dp_{\mathrm{GD}}$, $n = 1$	0.82	0.96×10^6
$x = 60dp_{\mathrm{GD}}$, $n = 1$	0.80	0.91×10^6
$x = 80dp_{\mathrm{GD}}$, $n = 1$	0.76	0.87×10^6
$x = 100dp_{\mathrm{GD}}$, $n = 1$	0.74	0.82×10^6
$x = 20dp_{\mathrm{GD}}$, $n = 0.5$	8.60	8.17×10^6
$x = 40dp_{\mathrm{GD}}$, $n = 0.5$	7.36	7.64×10^6
$x = 60dp_{\mathrm{GD}}$, $n = 0.5$	6.56	7.27×10^6
$x = 80dp_{\mathrm{GD}}$, $n = 0.5$	6.12	6.93×10^6
$x = 100dp_{\mathrm{GD}}$, $n = 0.5$	5.20	6.57×10^6

For the kinematics of the debris, using MESH-IN with n=1 resulted in low accuracy. For this reason, while $n = 1$ works well when only the hydrodynamics is considered, as can be seen in Table 9, $n < 1$ is suggested for when small waterborne debris are also modelled. Due to this, only results for $n = 0.5$ (see Fig. 9 and Fig. 10) are shown here in comparison with the GD simulation. In terms of trajectory, the use of $n = 0.5$ improves the results with respect to the GD in the y-direction, as the trajectories follow closely the mean experimental one. The only exception is for $60dp_{\mathrm{GD}}$, which is probably due to local features of the flow not being well represented by MESH-IN because of its positioning. It is stressed that the width of the flume is fairly larger than the debris dimensions, so that small local differences in the flow tip can significantly influence the debris dynamics. The effect of the location of MS is more noticeable for the x-trajectory for which the nRMSE$_l$ is calculated in Table 11. MESH-IN with n=0.5 improves the x-trajectory up to $40dp_{\mathrm{GD}}$, after which the accuracy oscillate for $60 < l < 80$ and it substantially decays for $x = 100dp_{\mathrm{GD}}$ especially in the x-direction trajectory. This decay is due to the progressively thinner flow, initially measured at the MS in the GD resulting in higher nRMSE$_l$. However, the maximum difference between the GD simulation and that using MESH-IN with the MS at $x = 100dp_{\mathrm{GD}}$ is only 7.9%. The nRMSE$_l$ for the trajectories with respect to the average experimental trajectory is shown in Table 11.

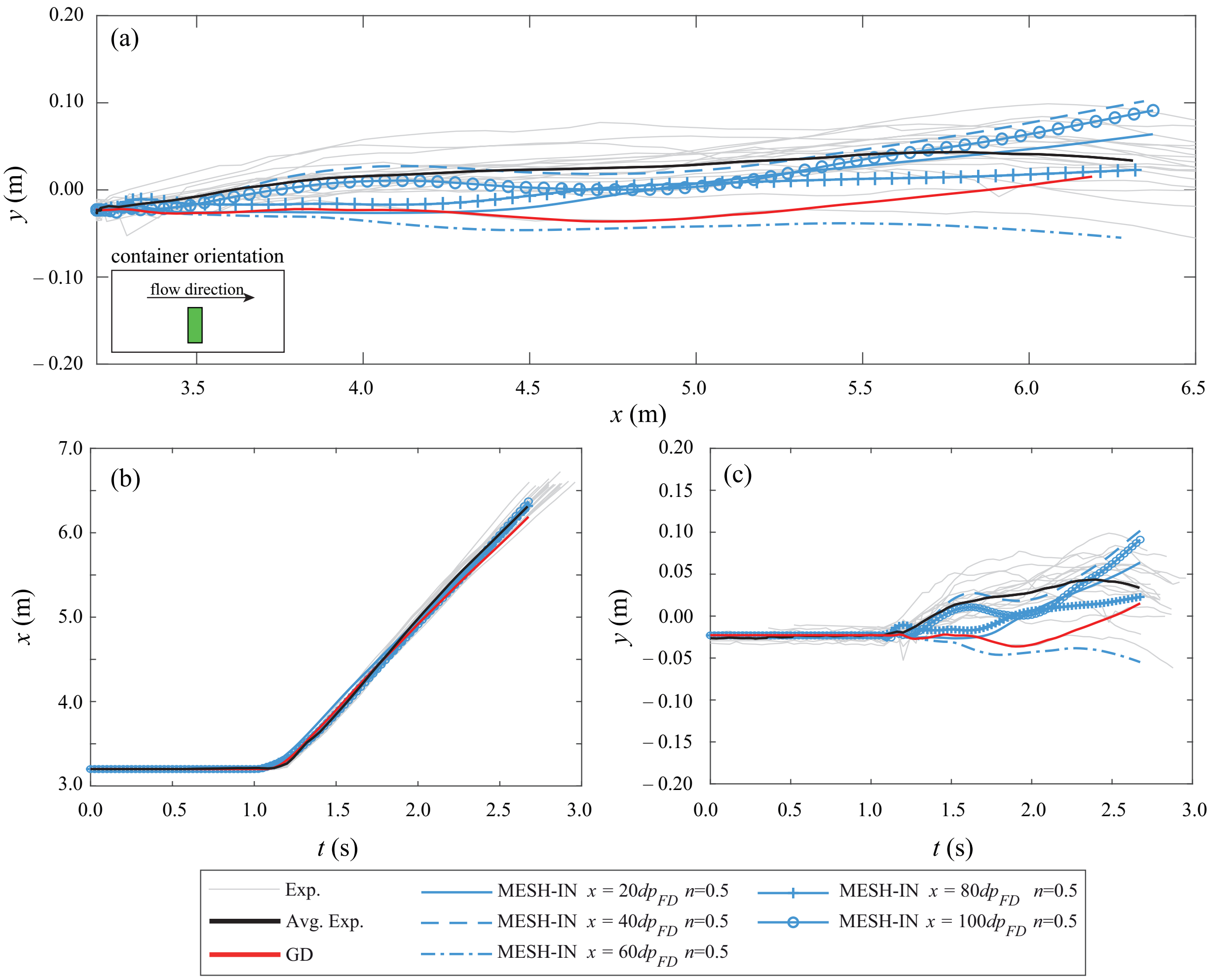

Figure 9: Comparison between experimental, GD and MESH-IN simulations of the debris trajectories (a) and their time evolution in x (b) and y-directions (c).

Similar behaviour can be obviously found for v_x and v_y as shown in Fig. 10. The only major difference between the GD and MESH-IN simulations is shown in Fig. 10a where the initial pick-up of the debris starts 0.075 s before for the MESH-IN simulation. After, v_x starts to follow again the mean experimental and GD v_x time series. However, this difference only slightly affects the overall performance, as shown in Table 11, where the maximum difference in nRMSE$_v$ is 0.035 between GD and MESH-IN simulations.

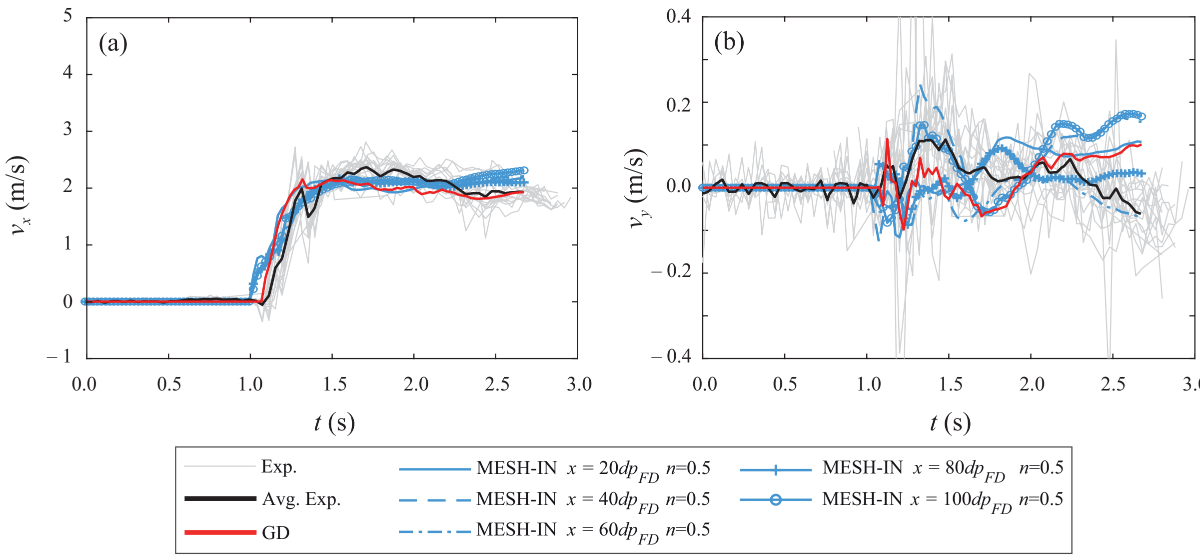

Figure 10: Comparison between experimental, GD and MESH-IN simulations of the debris velocities v_x (a) and v_y (b).

Table 11: nRMSE$_l$ and nRMSE$_v$ values for Experiment II simulations compared with experiments.

	$\boldsymbol{x}$	$\boldsymbol{y}$	$\boldsymbol{v_x}$	$\boldsymbol{v_y}$
GD	0.138	0.089	0.110	0.025
$x = 20dp_{\mathrm{GD}}$, $n = 0.5$	0.143	0.050	0.145	0.029
$x = 40dp_{\mathrm{GD}}$, $n = 0.5$	0.102	0.023	0.088	0.033
$x = 60dp_{\mathrm{GD}}$, $n = 0.5$	0.140	0.120	0.095	0.029
$x = 80dp_{\mathrm{GD}}$, $n = 0.5$	0.089	0.048	0.094	0.023
$x = 100dp_{\mathrm{GD}}$, $n = 0.5$	0.217	0.020	0.104	0.023

The positioning of the MS at $x = 40dp_{\mathrm{GD}}$ results in the best performance in terms of debris dynamics even when compared to the GD simulation. This is due to the better 3-D representation of the flow when using higher resolution. To assess this, Fig. 11 shows a qualitative comparison between the flow structure resulting from the experiments, GD, and MESH-IN with the MS at $x = 40dp_{\mathrm{GD}}$, from top to bottom. Fig. 11a,c,e are snapshots at $t = 1.56$ s, which show similar positioning of the debris compared to the experiments and very similar flow tip between the two simulations. However, it can be seen how the dam-break tip is better defined for the MESH-IN with $n = 0.5$. More differences between GD and MESH-IN with $n = 0.5$ are seen in Fig. 11b,d,f where in Fig. 11f the 3-D features of the experiments (highlighted with solid red lines in Fig. 11b) are very well captured while in Fig. 11d are almost absent. Velocity magnitudes ($|v|$) colour maps are also added to qualitatively compare the velocity fields between GD and MESH-IN simulations, showing very close correspondence especially for Fig. 11d and f.

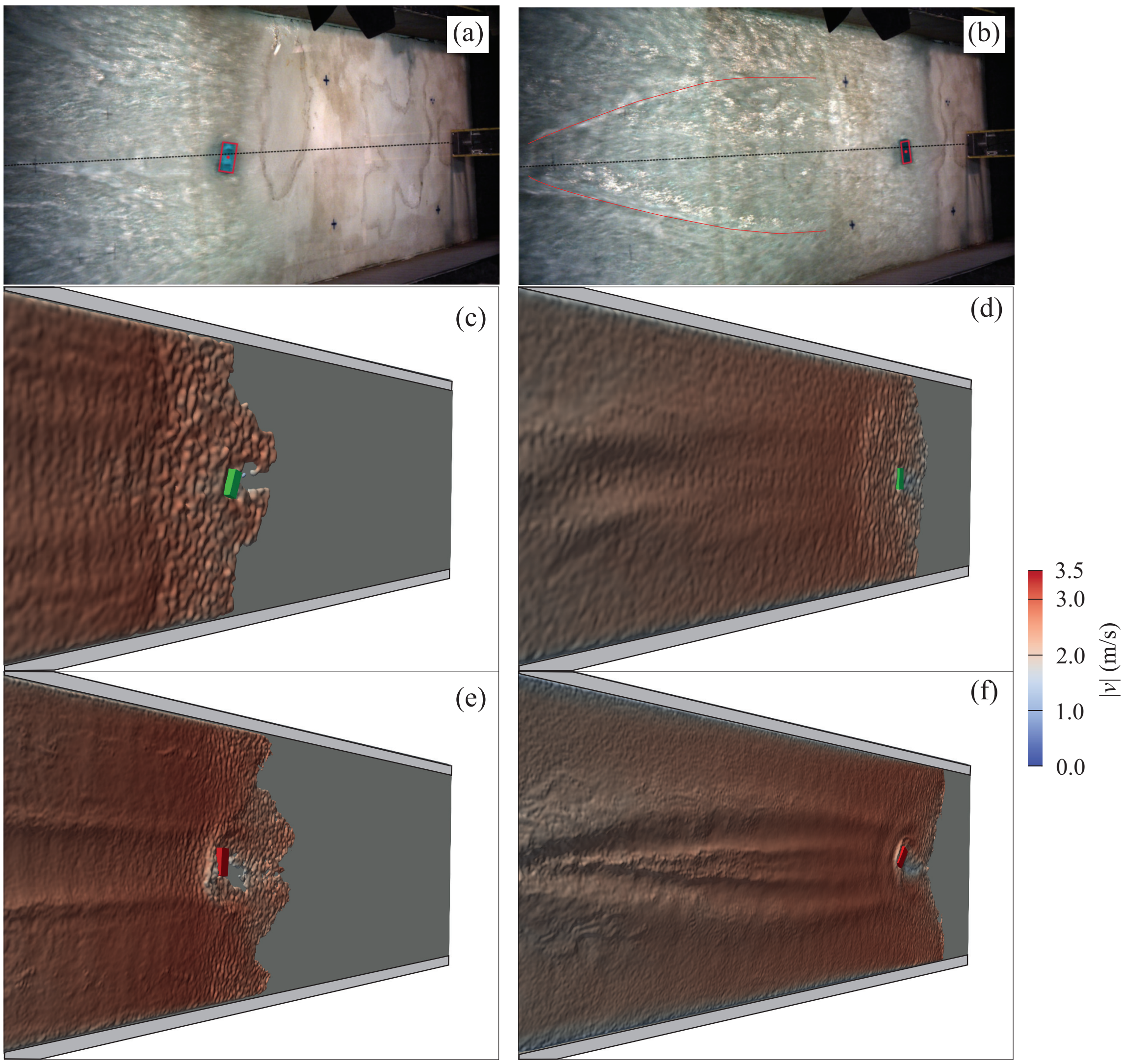

Figure 11: Comparison of the 3-D flow characteristics and debris movement between experiments (a,b), FP (c,d) and MESH-IN (e,f) at $x = 40dp_{\mathrm{GD}}$ and $n = 0.5$ at $t = 1.56$ s (a,c,e) and at $t = 2.40$ s (b,d,f). 3-D flow features are highlighted for the experiments with solid red lines.

5. Discussions

The results presented demonstrate that the MESH-IN offline coupling method is able to accurately reproduce h/h_0 when the MS is located in the range of $20dp_{\mathrm{GD}} < x < 100dp_{\mathrm{GD}}$. Note that, positions of $x < 0dp_{\mathrm{GD}}$ should not be used since significant flow delay occurs due to the MS measuring non zero velocities after the initiation of the flow. nRMSE_p show similar performances (see Table 8) than the nRMSE_l for h/h_0 with a slight decay by increasing l. Substantial improvements in resolving more complex hydrodynamic features were also found by increasing the resolution of the MS up to $n = 0.5$ above which these improvements become smaller if weighted against higher computational costs.

Due to its relatively small size with respect to the flow width, the tested debris was susceptible to small differences in the flow tip. This is a common occurrence for waterborne debris in flows of this type. For this reason Δ_{MS} smaller than GD simulations (n<1) are suggested for MESH-IN for more accurate results. The accuracy of the MESH-IN domain results for the container kinematics deteriorates with the position of the MS at $x \geq 40dp_{GD}$. For this reason, our study leads to $x = 40dp_{GD}$ as the optimal position of the MS in case of waterborne debris simulated. However, this should be considered as a first attempt positioning that should be further adjusted based on the characteristics of the particular simulated case. This highlights the need to accurately calibrate the value of l to find the best balance between accuracy and computational resources. Computational advantages are also found in applying MESH-IN, with the reduction by up to 17.6 times the time needed to simulate Experiment II with the same dp of the GD simulation, without negatively affecting the accuracy of the results. This reduction is by up to 2.5 times for MESH-IN simulations with $n = 0.5$ compared to the GD. However, in this case the performance of the container kinematics was even improved in some cases when compared to the experimental measurements. Note that the computational time might increase in MESH-IN simulations if compared to a GD one when a very high resolution is used. However, MESH-IN is seen in this study to allow for higher resolutions, e.g. $dp_{MESH-IN} = dp_{GD}/2$ or higher, that might not be possible by simulating the entire domain due to computational resources needed.

6. Conclusions

The new offline coupling method presented in this paper, referred to as MESH-IN, allows to investigate flows that are typical of extreme hydrodynamic events in domains with high resolution and/or reduce computational time by using results measured on a meshed surface (MS) from another larger full domain simulation (GD). This is very relevant for coastal applications especially in the context of tsunamis inundation. Additionally, since the associated flow is often supercritical, this coupling method allows for high flexibility with the possibility of modifying the downstream numerical setup without the need for simulating the large numerical domain each time.

The MESH-IN method was validated and compared against two different dam-break laboratory experiments in one of which debris transport was included. A sensitivity analysis on the effect of the positioning of the surface from the point of release of the dam-break and the spacing of its grid was carried out. This allowed to provide guidelines for the optimal positioning of the GD. In terms of hydrodynamics, the performance of MESH-IN is highest for the MS positioned between 20 and 100 times the GD resolution from the dam-break release position. Note that only a slight decay in performance for the MESH-IN simulations was seen with increasing distances, with a maximum difference of nRMSE_l=0.035 when compared to the GD simulation. For the debris kinematic it was found that MESH-IN positioning and resolution had a larger impact on the accuracy of the results. This led to a reduced optimal range of positions for the MS and by increasing its resolution it was possible to improve the accuracy in reproducing the mean experimental debris kinematics. The latter effect can be attributed to a more accurate 3-D representation of the flow downstream of the GD.

Additionally, this novel offline coupling method allows for substantial reduction (up to 17.6 times) of computational time with respect to GD simulations without decreasing results accuracy compared to experimental measurements, or even improving it for the container kinematics. This advantage might be also traded for higher resolution, therefore allowing for otherwise computationally unsustainable resolutions. Both aspects are very important as they make MESH-IN applicable to a wide range of scenarios. MESH-IN shares with offline coupling methods the limitation of not allowing feedback to the GD. However, it is meant to be used for scenarios where this type of coupling is not required. A further limitation, shared with coupling methods of all types, is that the accuracy of the boundary conditions depends on the GD simulations. This is a very important aspect for the present method since it relies on flow variables interpolation at the boundary, therefore care must be taken to obtain reliable GD simulations. Furthermore, the results presented here indicate that the use of the MS leads to differences at late stages of the flows simulated herein. Spurious oscillations in the free surface are introduced by the MESH-IN method, although their magnitude is not consistent across the cases studied. They are indeed more pronounced for the MESH-IN results for the reflected flow in Experiment I caused by the superposition of the incident and the reflected flow, this latter showing spray in the front region (see e.g. Fig. 7d). Noise in the free surface also appear in Experiment II in WG2 (see Fig. 8b, c), but not at WG3 (Fig. 8d, e).

In conclusion, the proposed method can be used effectively for offline coupling to simulate extreme 3-D hydrodynamic events in areas of interest, provided an assessment on the MS positioning and resolution is carried out. MESH-IN can also be applied as an offline variable resolution approach when dp is reduced. The validation tests showed that MESH-IN is able to take into account reflection. However, any downstream control of the flow at the MESH-IN location is frozen at the GD simulation. If characteristics of the downstream subdomain are changed (e.g. position, dimensions of obstacles), these are not updated. Therefore, when these changes are needed, MESH-IN use is limited to flows with no or negligible downstream control, e.g. supercritical flows or cases where reflection is negligible at the MS location. Validation tests demonstrated that changes in resolution do not affect the accuracy of the simulations negatively. For this reason, MESH-IN is particularly useful when analysing the flow close to structures and obstacles where retaining the 3-D accuracy with high resolutions is essential.

Acknowledgements

This research was supported by grants from NVIDIA and utilized NVIDIA RTX A6000 48GB. Dr. Corrado Altomare acknowledges funding from Spanish government and the European Social Found (ESF) under the programme 'Ramón y Cajal 2020' (RYC2020-030197-I / AEI / 10.13039/501100011033). This work was partially supported by the project SURVIWEC PID2020-113245RB-I00 financed by MCIN/AEI/10.13039/501100011033 and by the project ED431C 2021/44 "Programa de Consolidación e Estructuración de Unidades de Investigación Competitivas" financed by Xunta de Galicia, Consellería de Cultura, Educación e Universidade. This study forms part of the Marine Science programme (ThinkInAzul) supported by Ministerio de Ciencia e Innovación and Xunta de Galicia with funding from European Union NextGenerationEU (PRTR-C17.I1) and European Maritime and Fisheries Fund.

A. Mass and energy retainment between GD and MESH-IN simulations

Retainment of total mass m_{tot} and total energy E_{tot} between GD and MESH-IN results is demonstrated in this section. The time series of both quantities are compared using Experiment II and the results of MESH-IN for $x = 40dp_{GD}$ with $n = 0.5$ at three different positions using control volumes of $10dp_{GD}$ thickness and spanning the entire cross section of the flume. The positions analysed are right after the MESH-IN boundary condition at $x = 0.45$ m, at WG2 ($x = 2.0$m) and close to the container location at $x = 3.0$ m. The m_{tot} comparison is shown in Fig. A.1 where its value is calculated as:

$$m_{tot} = n_p dp^3 \rho_w \tag{A.1}$$

where n_p is the number of particles in the control volume in a given time, dp^3 is the particle volume in 3-D and ρ_w is the water density.

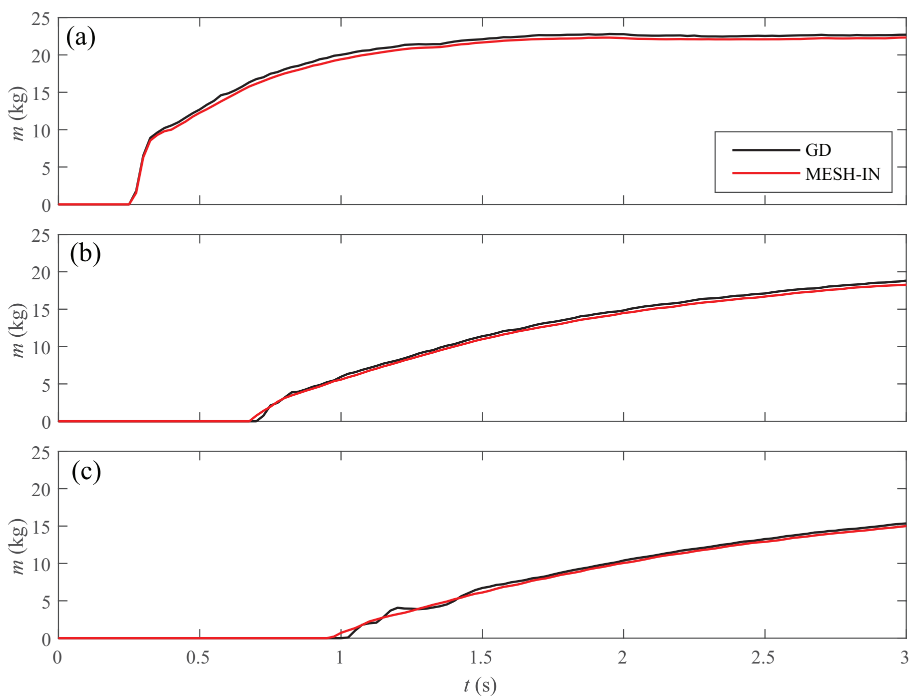

Figure A.1: Comparison of m_{tot} between GD and MESH-IN simulations of Experiment II for control volumes positioned at $x = 0.45$m (a), $x = 2.0$m (b), $x = 3.0$m (c).

Fig. A.2 shows the time series of the E_{tot} considered as the sum of the kinetic, potential and internal energy. As can be seen both GD and MESH-IN results show almost identical values for the entirety of the simulation.

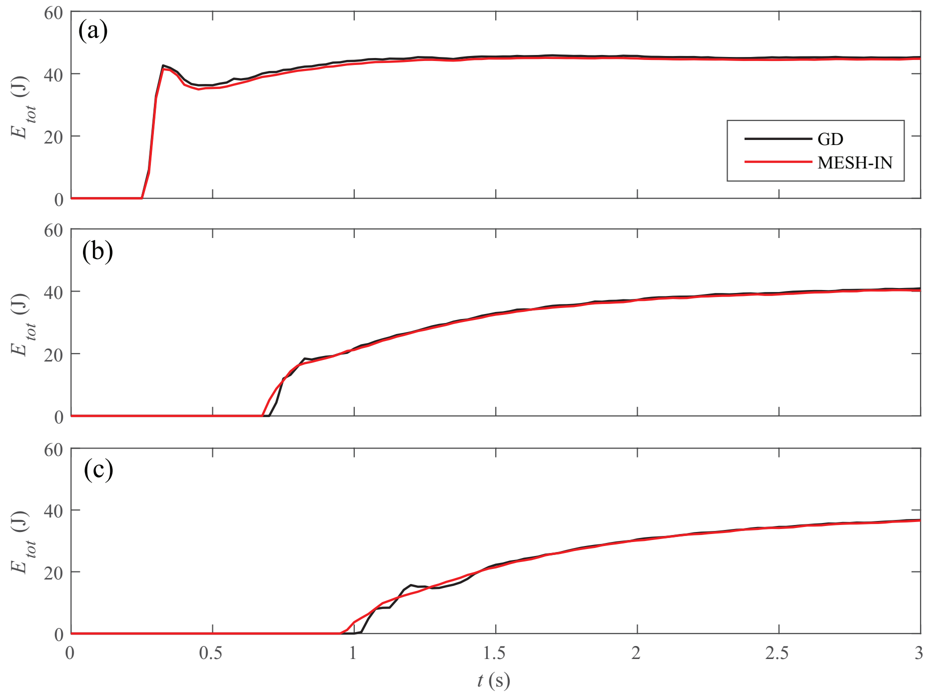

Figure A.2: Comparison of E_{tot} between GD and MESH-IN simulations of Experiment II for control volumes positioned at $x = 0.45$m (a), $x = 2.0$m (b), $x = 3.0$m (c).

References

Altomare, C., Domínguez, J., Crespo, A., Suzuki, T., Caceres, I., Gómez-Gesteira, M., 2015. Hybridization of the wave propagation model SWASH and the meshfree particle method SPH for real coastal applications. *Coastal Engineering Journal* 57(4), 1550024–1.

Altomare, C., Gironella, X., Crespo, A.J., 2021. Simulation of random wave overtopping by a WCSPH model. *Applied Ocean Research* 116, 102888.

Altomare, C., Tagliafierro, B., Dominguez, J., Suzuki, T., Viccione, G., 2018. Improved relaxation zone method in SPH-based model for coastal engineering applications. *Applied Ocean Research* 81, 15–33.

Anitescu, M., Tasora, A., 2010. An iterative approach for cone complementarity problems for nonsmooth dynamics. *Computational Optimization and Applications* 47(2), 207–235.

Areu-Rangel, O.S., Hernández-Fontes, J.V., Silva, R., Esperança, P.T., Klapp, J., 2021. Green water loads using the wet dam-break method and SPH. *Ocean Engineering* 219, 108392.

Canelas, R., Brito, M., Feal, O., Domínguez, J., Crespo, A., 2018. Extending DualSPHysics with a Differential Variational Inequality: Modeling fluid-mechanism interaction. *Applied Ocean Research* 76, 88–97.

Canelas, R., Domínguez, J., Crespo, A., Gómez-Gesteira, M., Ferreira, R., 2017. Resolved simulation of a granular-fluid flow with a coupled SPH-DCDEM model. *Journal of Hydraulic Engineering* 143(9), 06017012.

Canelas, R.B., Crespo, A.J., Dominguez, J.M., Ferreira, R.M., Gómez-Gesteira, M., 2016. SPH–DCDEM model for arbitrary geometries in free surface solid–fluid flows. *Computer Physics Communications* 202, 131–140.

Capasso, S., Tagliafierro, B., Güzel, H., Yilmaz, A., Dal, K., Kocaman, S., Viccione, G., Evangelista, S., 2021. A numerical validation of 3D experimental dam-break wave interaction with a sharp obstacle using DualSPHysics. *Water* 13(15), 2133.

Capasso, S., Tagliafierro, B., I., M.E., Domínguez, J., Crespo, A., Viccione, G., 2022. A dem approach for simulating flexible beam elements with the project chrono core module in dualsphysics. *Computational Particle Mechanics* 9(5), 969–985. doi:10.1007/s40571-021-00451-9.

Chanson, H., 2006. Tsunami surges on dry coastal plains: Application of dam break wave equations. *Coastal engineering journal* 48(04), 355–370.

Crespo, A., Gómez-Gesteira, M., Dalrymple, R.A., 2008. Modeling dam break behavior over a wet bed by a SPH technique. *Journal of waterway, port, coastal, and ocean engineering* 134(6), 313–320.

Crespo, A.J., Gómez-Gesteira, M., Dalrymple, R.A., 2007. Boundary conditions generated by dynamic particles in SPH methods. *Computers, materials and continua* 5(3), 173–184.

Domínguez, J., Crespo, A., Gómez-Gesteira, M., Marongiu, J., 2011. Neighbour lists in smoothed particle hydrodynamics. *International Journal for Numerical Methods in Fluids* 67(12), 2026–2042.

Domínguez, J.M., Crespo, A.J., Gómez-Gesteira, M., 2013. Optimization strategies for cpu and gpu implementations of a smoothed particle hydrodynamics method. *Computer Physics Communications* 184(3), 617–627.

Domínguez, J.M., Fourtakas, G., Altomare, C., Canelas, R.B., Tafuni, A., García-Feal, O., Martínez-Estévez, I., Mokos, A., Vacondio, R., Crespo, A.J., et al., 2022. DualSPHysics: From fluid dynamics to multiphysics problems. *Computational Particle Mechanics* 9(5), 867–895. doi:https://doi.org/10.1007/s40571-021-00404-2.

English, A., Domínguez, J., Vacondio, R., Crespo, A., Stansby, P., Lind, S., Chiapponi, L., Gómez-Gesteira, M., 2022. Modified dynamic boundary conditions (mDBC) for general-purpose smoothed particle hydrodynamics (SPH): application to tank sloshing, dam break and fish pass problems. *Computational Particle Mechanics* 9(5), 911–925. doi:https://doi.org/10.1007/s40571-021-00403-3.

Ferrand, M., Joly, A., Kassiotis, C., Violeau, D., Leroy, A., Morel, F.X., Rogers, B.D., 2017. Unsteady open boundaries for SPH using semi-analytical conditions and Riemann solver in 2D. *Computer Physics Communications* 210, 29–44.

Fourtakas, G., Dominguez, J.M., Vacondio, R., Rogers, B.D., 2019. Local uniform stencil (LUST) boundary condition for arbitrary 3-D boundaries in parallel Smoothed particle hydrodynamics (SPH) models. *Computers & Fluids* 190, 346–361.

Gaburro, E., Boscheri, W., Chiocchetti, S., Klingenberg, C., Springel, V., Dumbser, M., 2020. High order direct Arbitrary-Lagrangian-Eulerian schemes on moving Voronoi meshes with topology changes. *Journal of Computational Physics* 407, 109167.

Ganju, N.K., Brush, M.J., Rashleigh, B., Aretxabaleta, A.L., Del Barrio, P., Grear, J.S., Harris, L.A., Lake, S.J., McCardell, G., O'Donnell, J., et al., 2016. Progress and challenges in coupled hydrodynamic-ecological estuarine modeling. *Estuaries and Coasts* 39(2), 311–332.

Gomez-Gesteira, M., Rogers, B.D., Crespo, A.J., Dalrymple, R.A., Narayanaswamy, M., Dominguez, J.M., 2012. SPHysics–development of a free-surface fluid solver–part 1: Theory and formulations. *Computers & Geosciences* 48, 289–299.

Gomez-Gesteira, M., Rogers, B.D., Dalrymple, R.A., Crespo, A.J., 2010. State-of-the-art of classical SPH for free-surface flows. *Journal of Hydraulic Research* 48(sup1), 6–27.

González-Cao, J., Altomare, C., Crespo, A., Domínguez, J., Gómez-Gesteira, M., Kisacik, D., 2019. On the accuracy of DualSPHysics to assess violent collisions with coastal structures. *Computers & Fluids* 179, 604–612. URL: `https://www.sciencedirect.com/science/article/pii/S0045793018309022`.

Harper, C.A., 2000. Modern plastics handbook. McGraw-Hill Education.

Heller, V., Bruggemann, M., Spinneken, J., Rogers, B.D., 2016. Composite modelling of subaerial landslide–tsunamis in different water body geometries and novel insight into slide and wave kinematics. *Coastal Engineering* 109, 20–41.

Kocaman, S., Evangelista, S., Viccione, G., Güzel, H., 2020. Experimental and numerical analysis of 3D dam-break waves in an enclosed domain with a single oriented obstacle, *in: Environmental Sciences Proceedings*. 2(1), Multidisciplinary Digital Publishing Institute, 35.

Lauber, G., Hager, W.H., 1998. Experiments to dambreak wave: Horizontal channel. *Journal of Hydraulic research* 36(3), 291–307.

Liu, G.R., Liu, M.B., 2003. Smoothed particle hydrodynamics: A meshfree particle method. World scientific.

Liu, M., Liu, G.R., 2006. Restoring particle consistency in smoothed particle hydrodynamics. *Applied numerical mathematics* 56(1), 19–36.

Ma, Z., Qian, L., Martinez-Ferrer, P., Causon, D., Mingham, C., Bai, W., 2018. An overset mesh based multiphase flow solver for water entry problems. *Computers & Fluids* 172, 689–705.

Michael, L.B., 1991. SPI Plastics Engineering Handbook of the Society of the Plastics Industry. Springer: New York, NY, USA.

Monaghan, J.J., 1992. Smoothed particle hydrodynamics. *Annual review of astronomy and astrophysics* 30(1), 543–574.

Naito, C., Cercone, C., Riggs, H., Cox, D., 2014. Procedure for site assessment of the potential for tsunami debris impact. *Journal of Waterway, Port, Coastal, and Ocean Engineering* 140(2), 223–232.

Ni, X., Feng, W., Huang, S., Zhao, X., Li, X., 2020. Hybrid SW-NS SPH models using open boundary conditions for simulation of free-surface flows. *Ocean Engineering* 196, 106845.

Novak, G., Tafuni, A., Domínguez, J.M., Četina, M., Žagar, D., 2019. A numerical study of fluid flow in a vertical slot fishway with the Smoothed particle hydrodynamics method. *Water* 11(9), 1928.

Peskin, C.S., 2002. The immersed boundary method. *Acta numerica* 11, 479–517.

Pons, J.P., Boissonnat, J.D., 2007. Delaunay deformable models: Topology-adaptive meshes based on the restricted delaunay triangulation, *in: 2007 IEEE Conference on Computer Vision and Pattern Recognition*, IEEE, 1–8.

Romano, A., Lara, J., Barajas, G., Di Paolo, B., Bellotti, G., Di Risio, M., Losada, I., De Girolamo, P., 2020. Tsunamis generated by submerged landslides: Numerical analysis of the near-field wave characteristics. *Journal of Geophysical Research: Oceans* 125(7), e2020JC016157.

Ruffini, G., Briganti, R., De Girolamo, P., Stolle, J., Ghiassi, B., Castellino, M., 2021. Numerical modelling of flow-debris interaction during extreme hydrodynamic events with DualSPHysics-CHRONO. *Applied Sciences* 11(8), 3618.

Stolle, J., Ghodoosipour, B., Derschum, C., Nistor, I., Petriu, E., Goseberg, N., 2018a. Swing gate generated dam-break waves. *Journal of Hydraulic Research* .

Stolle, J., Goseberg, N., Nistor, I., Petriu, E., 2018b. Probabilistic investigation and risk assessment of debris transport in extreme hydrodynamic conditions. *Journal of Waterway, Port, Coastal, and Ocean Engineering* 144(1), 04017039.

Suzuki, T., García-Feal, O., Domínguez, J.M., Altomare, C., 2022. Simulation of 3D overtopping flow–object–structure interaction with a calibration-based wave generation method with DualSPHysics and SWASH. *Computational Particle Mechanics* 9(5), 1003–1015. doi:https://doi.org/10.1007/s40571-022-00468-8.

Tafuni, A., Domínguez, J., Vacondio, R., Crespo, A., 2018. A versatile algorithm for the treatment of open boundary conditions in Smoothed particle hydrodynamics GPU models. *Computer Methods in Applied Mechanics and Engineering* 342, 604–624.

Tagliafierro, B., Mancini, S., Ropero-Giralda, P., Domínguez, J.M., Crespo, A.J., Viccione, G., 2021. Performance assessment of a planing hull using the Smoothed Particle Hydrodynamics method. *Journal of Marine Science and Engineering* 9(3), 244.

Tan, H., Ruffini, G., Heller, V., Chen, S., 2018. A numerical landslide-tsunami hazard assessment technique applied on hypothetical scenarios at Es Vedrà, offshore ibiza. *Journal of Marine Science and Engineering* 6(4), 111.

Tasora, A., Anitescu, M., 2011. A matrix-free cone complementarity approach for solving large-scale, nonsmooth, rigid body dynamics. *Computer Methods in Applied Mechanics and Engineering* 200(5-8), 439–453.

Vacondio, R., Altomare, C., De Leffe, M., Hu, X., Le Touzé, D., Lind, S., Marongiu, J.C., Marrone, S., Rogers, B.D., Souto-Iglesias, A., 2021. Grand challenges for Smoothed Particle Hydrodynamics numerical schemes. *Computational Particle Mechanics* 8(3), 575–588.

Vacondio, R., Mignosa, P., Pagani, S., 2013. 3D SPH numerical simulation of the wave generated by the Vajont rockslide. *Advances in water resources* 59, 146–156.

Verbrugghe, T., Domínguez, J.M., Altomare, C., Tafuni, A., Vacondio, R., Troch, P., Kortenhaus, A., 2019. Non-linear wave generation and absorption using open boundaries within DualSPHysics. *Computer Physics Communications* 240, 46–59.

Violeau, D., Rogers, B.D., 2016. Smoothed particle hydrodynamics (SPH) for free-surface flows: past, present and future. *Journal of Hydraulic Research* 54(1), 1–26.

Wendland, H., 1995. Piecewise polynomial, positive definite and compactly supported radial functions of minimal degree. *Advances in computational Mathematics* 4(1), 389–396.

Xu, X., Jiang, Y.L., Yu, P., 2021. SPH simulations of 3D dam-break flow against various forms of the obstacle: Toward an optimal design. *Ocean Engineering* 229, 108978.

Zijlema, M., Stelling, G., Smit, P., 2011. SWASH: An operational public domain code for simulating wave fields and rapidly varied flows in coastal waters. *Coastal Engineering* 58(10), 992–1012.